JCB Journal of Cell Biology

ARTICLE

YAP and TAZ limit cytoskeletal and focal adhesion maturation to enable persistent cell motility

Devon E. Mason[1,2,3], Joseph M. Collins[1,2], James H. Dawahare[3], Trung Dung Nguyen[3,4], Yang Lin[5], Sherry L. Voytik-Harbin[6,7], Pinar Zorlutuna[3], Mervin C. Yoder[5], and Joel D. Boerckel[1,2,3]

Cell migration initiates by traction generation through reciprocal actomyosin tension and focal adhesion reinforcement, but continued motility requires adaptive cytoskeletal remodeling and adhesion release. Here, we asked whether de novo gene expression contributes to this cytoskeletal feedback. We found that global inhibition of transcription or translation does not impair initial cell polarization or migration initiation, but causes eventual migratory arrest through excessive cytoskeletal tension and over-maturation of focal adhesions, tethering cells to their matrix. The transcriptional coactivators YAP and TAZ mediate this feedback response, modulating cell mechanics by limiting cytoskeletal and focal adhesion maturation to enable persistent cell motility and 3D vasculogenesis. Motile arrest after YAP/TAZ ablation was partially rescued by depletion of the YAP/TAZ-dependent myosin phosphatase regulator, NUAK2, or by inhibition of Rho-ROCK-myosin II. Together, these data establish a transcriptional feedback axis necessary to maintain a responsive cytoskeletal equilibrium and persistent migration.

Introduction

Cells are equipped with cytoskeletal and adhesion machinery that enable motility in response to physical cues communicated at cell–cell and cell–matrix interfaces. Migration is driven by actomyosin force generation, which coordinates focal adhesion (FA) formation, reinforcement, and disassembly (Chan and Odde, 2008; Elosegui-Artola et al., 2016; Wu et al., 2017). These machinery form a molecular clutch, comprising abundantly expressed proteins capable of producing intracellular tension, cellular polarization, and motility, enabling rapid cellular responses to dynamic stimuli. Cytoskeletal activation also induces mechanosensitive transcriptional programs, but how transcription regulates migration is incompletely understood. Here, we identify a role for transcriptional feedback in actomyosin control of cell migration.

Actomyosin tension is important for forward motility, but alone cannot not produce persistent migration, which requires coordinated actin treadmilling, leading edge adhesion formation, and trailing edge disassembly (Kolega, 2003; Ezratty et al., 2005; Gupton and Waterman-Storer, 2006). Thus, negative feedback systems are inherent to migration. For instance, myosin light chain phosphatase (e.g., MLCP) modulates myosin motor activity to tune cytoskeletal tension (Totsukawa et al., 2004; Zagórska et al., 2010; Vallenius et al., 2011), while FA kinase (FAK) regulates adhesion remodeling (Shen et al., 2005).

The paralogous transcriptional coactivators yes-associated protein (YAP) and transcriptional coactivator with PDZ-binding motif (TAZ or WWTR1) have emerged as important mechanotransducers that couple biophysical cell–cell and cell–matrix cues to mechanotransductive gene expression (Dupont et al., 2011). YAP/TAZ activity is regulated by subcellular localization, and their nuclear accumulation is induced by tension of the actomyosin cytoskeleton (Dupont et al., 2011; Wada et al., 2011). These observations position YAP and TAZ as potential key mediators of cytoskeleton-induced transcriptional programs.

Endothelial colony-forming cells (ECFCs) are blood-circulating endothelial cells (Asahara et al., 1997) that exhibit high proliferative and motile capacity and contribute to endothelium repair in vivo (Ingram et al., 2004, 2005). When cultured in 3D matrices in vitro or transplanted in vivo, ECFCs have vasculogenic activity, characterized by cytoplasmic vacuolation, lumenization, and inosculation with host vasculature (Bailey et al., 2011; Whittington et al., 2013; Medina et al., 2017). Here,

[1]McKay Orthopaedic Research Laboratory, Department of Orthopedic Surgery, University of Pennsylvania, Philadelphia, PA; [2]Department of Bioengineering, University of Pennsylvania, Philadelphia, PA; [3]Department of Aerospace and Mechanical Engineering, University of Notre Dame, Notre Dame, IN; [4]Department of Engineering and Computer Science, Seattle Pacific University, Seattle, WA; [5]Herman B. Wells Center for Pediatric Research, Indiana University, Indianapolis, IN; [6]Weldon School of Biomedical Engineering, Purdue University, West Lafayette, IN; [7]Department of Basic Medical Sciences, Purdue University, West Lafayette, IN.

Correspondence to Joel D. Boerckel: boerckel@pennmedicine.upenn.edu.

we used ECFCs as a model system to test the importance of new gene expression for persistent cell migration and identify YAP and TAZ as mechanosensitive mediators of a transcriptional feedback loop that modulates cytoskeletal tension and FA formation. We found that YAP and TAZ prevent myosin-dependent motile arrest by negatively regulating myosin light chain phosphorylation to enable persistent cell motility. Physiologically, YAP and TAZ were essential for neovascular tube formation, 3D vacuolation, and neovascular sprouting.

Results

Transcription is essential for migration and regulates stress fiber and FA maturation

To evaluate directed motility driven by cell–cell and cell–matrix interactions in response to contact-inhibition release, we tracked cell migration over 8 h using the monolayer wound assay (Fig. 1 A). To decouple the action of existing cytoskeletal function from de novo gene products, we quantified longitudinal wound closure and wound migration rate in the presence of vehicle (DMSO) or inhibitors that prevent mRNA transcription (actinomycin D; 0.1 or 0.25 µg/ml) or protein translation (puromycin; 1 µg/ml), applied 1 h before migration initiation (Fig. 1 A). In vehicle-treated cells, wound closure rate reached a plateau, or migratory equilibrium, in ∼2 h. Transcription inhibition significantly reduced wound closure percentage and rate by 8 h after contact inhibition release (Fig. 1 B), while translation inhibition significantly slowed migration after 2 h, leading to motile arrest by 8 h.

One possible explanation for delayed loss of cell motility after transcription inhibition is depletion of cytoskeletal components over time. To test this, we evaluated actin polymerization and FA formation by immunofluorescence in leading edge cells. Rather than observing depletion of cytoskeletal components, transcription/translation inhibition significantly increased stress fiber formation (Fig. 1 C), actin polymerization (Fig. 1, D–F), and FA maturation (Fig. 1, G and H). Relative filamentous and monomeric actin quantity was computed as F- or G-actin intensity, normalized to control cell intensity, on a per-cell basis (by phalloidin and DNase I, respectively). Prolonged transcription inhibition significant increased F-actin intensity, but did not affect G-actin intensity (Fig. 1 D). Rather, the fraction of filamentous actin (i.e., F-/G-actin) was significantly increased by both inhibitors (Fig. 1, D–F). Vinculin recruitment to FAs, measured as FA length, was significantly increased by transcription or translation inhibition (Fig. 1 H).

Thus, rather than depleting the migratory machinery, inhibition of new gene expression led to abundant cytoskeletal tension and increased FA maturation. This suggests a transcriptional feedback mechanism that modulates cytoskeletal tension and FA dynamics to enable persistent migration.

YAP and TAZ are mechanosensitive in ECFCs

Recent evidence has identified the transcriptional coactivators, YAP and TAZ, as cytoskeletal tension-activated regulators of gene expression (Dupont et al., 2011). Therefore, we hypothesized that YAP and TAZ mediate this transcriptional feedback. First, we confirmed that YAP and TAZ are mechanosensors of cytoskeletal tension in ECFCs using collagen-coated extracellular matrices of variable rigidity. Cells were seeded in sparse (8,500 cells/cm^2) conditions on soft (1.85 kPa) or stiff (29 kPa) polyacrylamide (PA) or glass overnight followed by fixation and visualization of YAP and TAZ localization by immunocytochemistry (Fig. S1 A). Consistent with prior reports in other cell types (Dupont et al., 2011), increased substrate rigidity significantly increased spread cell area and elongation (Fig. S1, B and C) and increased nuclear localization of both YAP and TAZ (Fig. S1 D).

YAP and TAZ cell-autonomously regulate migration and cytoskeletal prestress

YAP/TAZ subcellular localization is regulated by cell–cell interactions through the Hippo pathway (Lei et al., 2008) and by cell–matrix interactions through cytoskeletal tension associated with cell spreading (Dupont et al., 2011; Wada et al., 2011; Bergert et al., 2016).

To track these interactions during cell migration, we quantified cell density and area as a function of position relative to the original wound edge, 10 h after migration initiation (Fig. 2, A and B; and Fig. S1 E). Cell density remained constant in the cell monolayer at distances >500 µm behind the wound edge, but dropped near the leading edge (Fig. 2 A). Spread cell area similarly increased, but the effect of the wound on spread area extended only 200 µm into the monolayer. Total (Fig. 2 C) and nuclear (Fig. 2 D) YAP and TAZ fluorescent intensity increased preferentially in migrating cells beyond the original wound edge (Fig. 2, C and D). The increase in total YAP/TAZ levels could be explained by increased expression, increased translation efficiency, or by stabilization from proteasomal degradation (Lei et al., 2008; Moroishi et al., 2015). However, *YAP/TAZ* mRNA levels were not altered after contact inhibition release (Fig. S2, A and B).

To test the combinatorial roles of YAP/TAZ in cell motility, we depleted *YAP* and/or *TAZ* using RNAi, reducing protein expression to 27 and 18% of scrambled siRNA controls, respectively (Fig. 2 E; and Fig. S2, C and D). Control cells closed the 0.5-mm-wide gaps within 12 h, but YAP and/or TAZ depletion significantly impaired wound closure, with TAZ and YAP/TAZ depletion nearly abrogating migration (Fig. 2, F and G; and Fig. S2 E). YAP/TAZ depletion significantly reduced mRNA expression of secreted growth factors and enzymes including *CTGF*, *Cyr61*, and *SERPINE1* (Fig. S2, F and H). This suggested that YAP/TAZ activation could stimulate cell migration by induction of secreted angiocrines. However, recombinant reconstitution of these proteins failed to rescue cell motility (Fig. S2, G and I) and transposition of conditioned medium from either control or YAP/TAZ-depleted cells (Fig. 2 H) similarly had no effect on either control or YAP/TAZ-depleted cell motility ($P = 0.99$; Fig. 2 I), suggesting a cell-intrinsic mechanism. Additionally, inhibition of proliferation using the DNA cross-linking agent, mitomycin C (mito C), had no effect on wound closure in either control or YAP/TAZ-depleted cells ($P > 0.30$; Fig. S2 J).

Intracellular mechanics dynamically respond to extracellular stimuli like contact inhibition release during migration (Wang

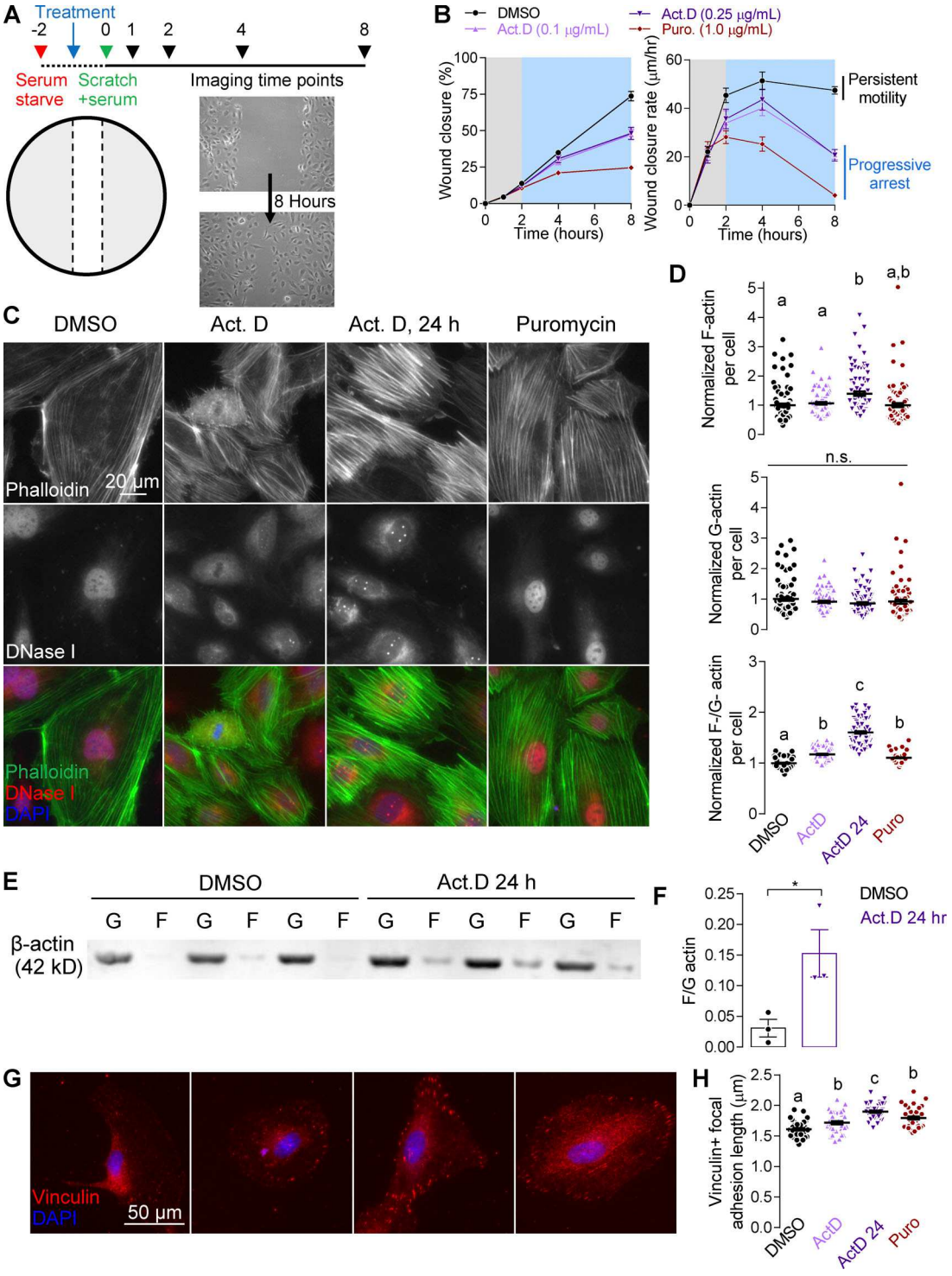

Figure 1. **De novo gene expression is essential for actin cytoskeleton and FA dynamics during migration**. **(A)** Confluent ECFCs were serum starved for 2 h, and actinomycin D or puromycin were added 1 h into the serum starve to inhibit transcription and translation, respectively. Monolayers were scratched to form an open "wound" to longitudinally quantify migratory closure. **(B)** Wound closure percentage, measured as (initial wound area − wound area at 8 h)/initial wound area × 100, and wound closure rate, measured as the distance the cell front moved over each imaging period (μm/h). Background color shows de novo gene expression–independent (gray) and –dependent (blue) phases. n = 19–24; $P < 0.025$; two-way ANOVA with Tukey's post hoc test. **(C)** F- and G-actin visualized by Alex Fluor 488 phalloidin, Alexa Fluor 594 DNase I, and nuclei visualized by DAPI. **(D)** Normalized F-actin and G-actin intensity and F-/G-actin ratio per cell, normalized to DMSO-treated controls. n = 60 cells; $P < 0.0001$; Kruskal Wallace with Dunn's post hoc test. **(E)** Western blot of β-actin in F- and G-fractions of ECFC lysate 24 h after actinomycin D. **(F)** F-/G-actin ratio of β-actin densitometry measurements in F- and G-fractions. n = 3 samples; $P < 0.04$; two-tailed Student's unpaired t test. **(G)** Vinculin and nuclei visualized by Alexa Fluor 594 secondary and DAPI. **(H)** Vinculin$^+$ FA length. n = 40 cells; $P < 0.009$; ANOVA with Tukey's post hoc test. Repeated significance indicator letters (e.g., a–a) signify $P > 0.05$, while groups with distinct indicators (a vs. b) signify $P < 0.05$. Summary statistics are represented as mean ± SEM. Box plots show interquartile range with whiskers at minimum/maximum. n.s., not significant; $P > 0.05$.

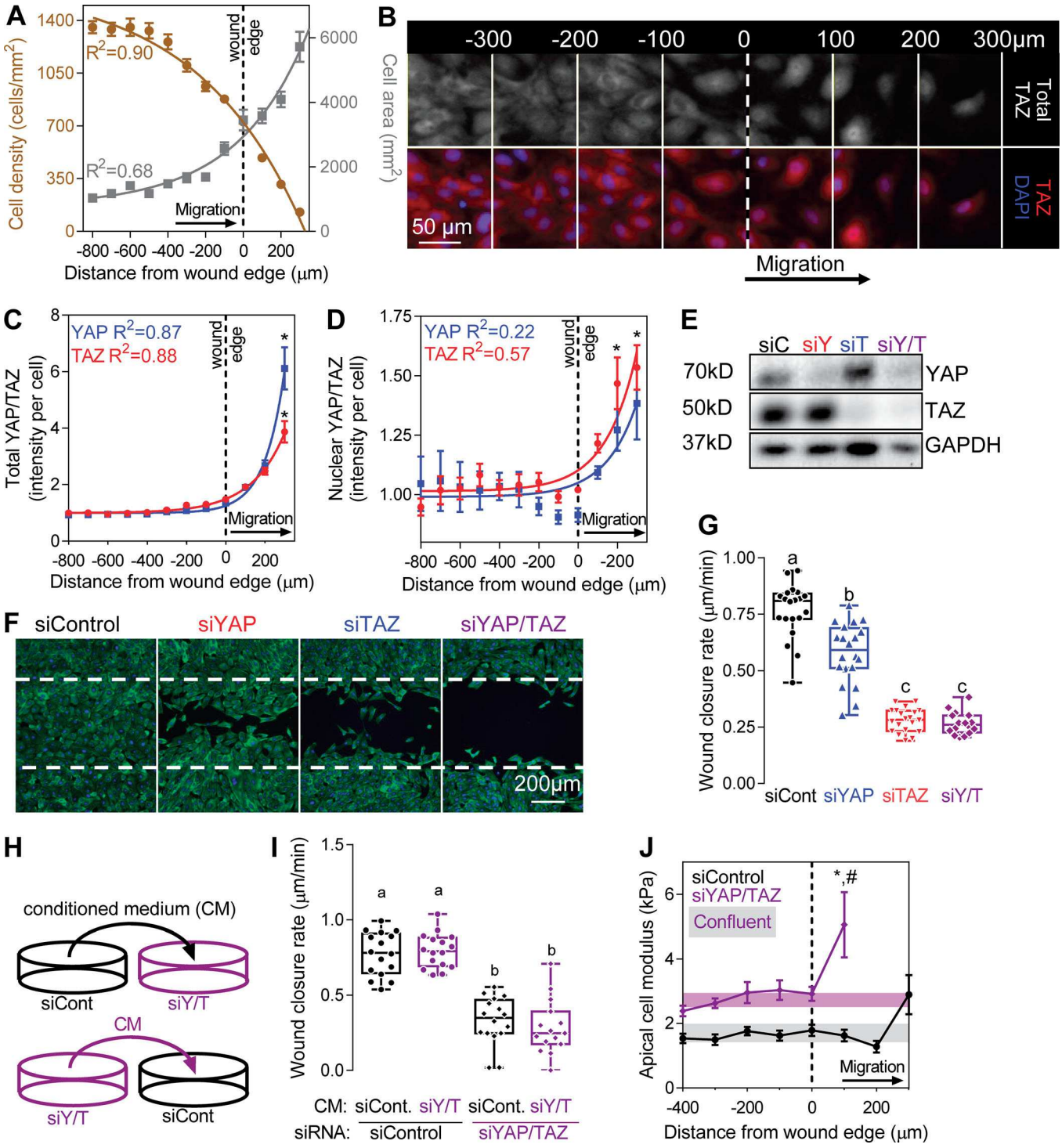

Figure 2. **YAP and TAZ are essential for ECFC motility by limiting cytoskeletal prestress. (A)** Average cell density ($y = -1863e^{-.00177x} + 1643$) and area ($y = 7062 - 6287[1 - e^{-.00267x}]$) as a function of distance from the leading edge (dotted lines) in 100-μm ROIs. **(B)** TAZ localization visualized by Alexa Fluor 594 secondary and DAPI subdivided into 100-μm ROIs. **(C)** Normalized total YAP ($y = .255e^{-.00996} + 1$ and TAZ ($y = .486e^{-.00582x} + 1$) fluorescent intensity. **(D)** Normalized nuclear YAP ($y = .003e^{-.00839x} + 1$) and TAZ ($y = .120e^{-.00529x} + 1$) fluorescent intensity. $n = 7$; *, $P < 0.0001$ versus all other ROIs; two-way ANOVA with Tukey's post hoc test. **(E)** Confirmation of YAP and TAZ depletion by Western blot. **(F)** ECFC migration; actin visualized by Alexa Fluor 488 phalloidin. **(G)** Wound closure rate. $n = 16–20$; $P < 0.0001$; ANOVA with Tukey's post hoc test. **(H)** Conditioned medium from siControl or siYAP/TAZ was transferred to adjacent wells with siControl or siYAP/TAZ cells. **(I)** Wound closure after conditioned media treatment. $n = 16$; $P < 0.0001$; ANOVA with Tukey's post hoc test. **(J)** Apical cell modulus measured by nanoindentation at 100-μm ROIs. $n = 10–32$ cells per ROI; *, $P < 0.023$ versus control leading edge; #, $P < 0.001$ versus siYAP/TAZ monolayer; two-way ANOVA with Tukey's post hoc test.

et al., 2002; Polte et al., 2004; Roan et al., 2015) and drive YAP/TAZ nuclear localization (Dupont et al., 2011; Bergert et al., 2016). The collective stress imposed by myosin motors on bundled actin fibers is referred to as cellular prestress and can be quantified as apical cell modulus, measured by single-cell nanoindentation (Wang et al., 2002). We measured apical modulus as a function of migratory distance (Fig. 2 J). In control cells, apical modulus was elevated at the leading edge of the migrating front (Fig. 2 J), consistent with tension-induced YAP/TAZ activation (compare Fig. 2 D). YAP/TAZ-depleted cells exhibited reduced migration as above, but featured significantly elevated cell modulus compared with controls, both in the monolayer and at the leading edge (Fig. 2 J).

YAP and TAZ enable ECFC migration and directional persistence

Next, we evaluated collective and single-cell motility by live cell imaging (Fig. 3 and Videos 1, 2, and 3). Control cells migrated directionally, whereas YAP/TAZ-depleted cells remained tethered in place without persistent motion beyond the original cell borders (Fig. 3 A). Instantaneous, scalar cell migration speed was evaluated on a single-cell basis both for cells at the leading edge and in trailing cells, whose motility depends on contact inhibition release by motion of the leading cells. Control cell migration speed (in both leading and trailing cells) peaked 15 min after wounding and decreased to a minimum after 2 h (Fig. 3 B) before reaccelerating until experiment completion at 10 h. In contrast, YAP/TAZ-depleted cell migration speed was initially lower and then decreased continuously until hour 10. YAP/TAZ depletion significantly slowed migration regardless of leading or trailing position (Fig. 3 C).

Wound repair and directed angiogenesis in vivo require not only cell movement, but directional migration (Gerhardt et al., 2003). We therefore quantified instantaneous directionality of individual cells both at the leading edge and in the trailing monolayer. Directionality was defined for each 15-min time interval as the angle, $\varphi(t_n - t_{n-1})$, relative to the wound edge, between an individual cell position at time t_n and its prior position at time t_{n-1} (Fig. 3 D). Leading edge control cells migrated forward, while trailing cells lagged by 2 h, coinciding with the inflection in migration speed (compare Fig. 3 B) and the time at which transcription inhibition began to reduce cell motility (compare Fig. 1 B). In contrast, YAP/TAZ-depleted cells had a zero average directionality (Fig. 3 E) and reduced persistence, defined as the ratio of net migration distance to total distance traveled (Fig. 3 F).

We next asked whether individual YAP/TAZ-depleted cell motility could be restored by control cell contact. YAP/TAZ-depleted cells were plated sparsely in a 100-fold excess of control cells and random migration within the mixed monolayer was tracked over time in 2D space (Fig. 3 G). YAP/TAZ depletion significantly reduced individual cell motility by 43–47%, measured by mean square displacement (Fig. 3 H) and decreased net displacement (Fig. 3 I) compared with control cells in the same mixed monolayer. These data further support a cell-autonomous role of YAP and TAZ in cell migration.

YAP and TAZ are dispensable for microtubule polarization and Golgi reorientation

Cell migration initiates by establishment of front-rear cell polarity, determining motile direction (Kolega, 2003). Cellular polarization requires polarization of the microtubule-organizing center (MTOC) to coordinate microtubule extension and cytoskeletal remodeling and is accompanied by Golgi apparatus polarization (Kupfer et al., 1982). To determine whether YAP and TAZ regulate migratory cell polarity, we evaluated microtubule network structure and Golgi polarization, defined as orientation of the Golgi apparatus within ±60° of the direction of the wound (Fig. 4, A and B). Both control and YAP/TAZ-depleted cells had similar microtubule networks that extended from the MTOC to the cell periphery (Fig. 4 F), and YAP/TAZ depletion had no effect on Golgi polarization in leading edge cells (Fig. 4 C). 60% of cells at the migratory front featured polarized Golgi in either condition, significantly greater than the random (33%) distribution in nonwounded monolayers (Fig. 4 E). In the trailing region (Fig. 4 D), control cells had significant Golgi polarization, but YAP/TAZ-depleted trailing cells did not ($P = 0.81$; Fig. 4 E). These data suggest that YAP/TAZ are dispensable for direction sensing and the initiation of motile cell polarization, but are required for directional persistence.

YAP and TAZ regulate cytoskeletal and FA remodeling

We found that transcription inhibition caused migratory arrest and increased cytoskeletal polymerization and FA formation. Similarly, YAP/TAZ depletion impaired persistent migration and increased cellular prestress. We therefore hypothesized that YAP and TAZ transcriptionally regulate actin cytoskeletal architecture to enable persistent motility.

Consistent with this, YAP and/or TAZ depletion from migrating cells significantly increased stress fiber size and intensity (Fig. 5, A and B). YAP and/or TAZ depletion had no effect on normalized, single-cell, F- or G-actin intensity (Fig. 5 D); however, YAP and/or TAZ depletion significantly increased F- and G-actin intensity ratio (Fig. 5 E).

To test whether YAP and TAZ mediate cytoskeletal feedback in another primary cell type, and in a different context, we examined cytoskeletal architecture in differentiating bone marrow stromal cells (BMSCs) isolated from Osterix-conditional *YAP/TAZ* knockout mice (Kegelman et al., 2018). As previously described, osteogenic differentiation of BMSCs induces expression of the transcription factor Osterix (Kegelman et al., 2018). In these cells, homozygous recombination of floxed exon 3 of both *YAP* and *TAZ* results in frame shift and premature stop-induced–conditional deletion. Using this model, we induced differentiation of BMSCs toward an osteoprogenitor lineage for 14 d (Kegelman et al., 2018). Perinuclear stress fibers, measured by line scan intensity across single cells, were significantly increased after *YAP* and *TAZ* deletion (Fig. 5, F and G). These results are consistent with our findings in ECFCs and suggest YAP and TAZ limit cytoskeletal maturation in multiple cell types using orthogonal loss-of-function approaches.

Cell motility requires formation of new FAs at the cell's leading edge and coordinated adhesion disassembly

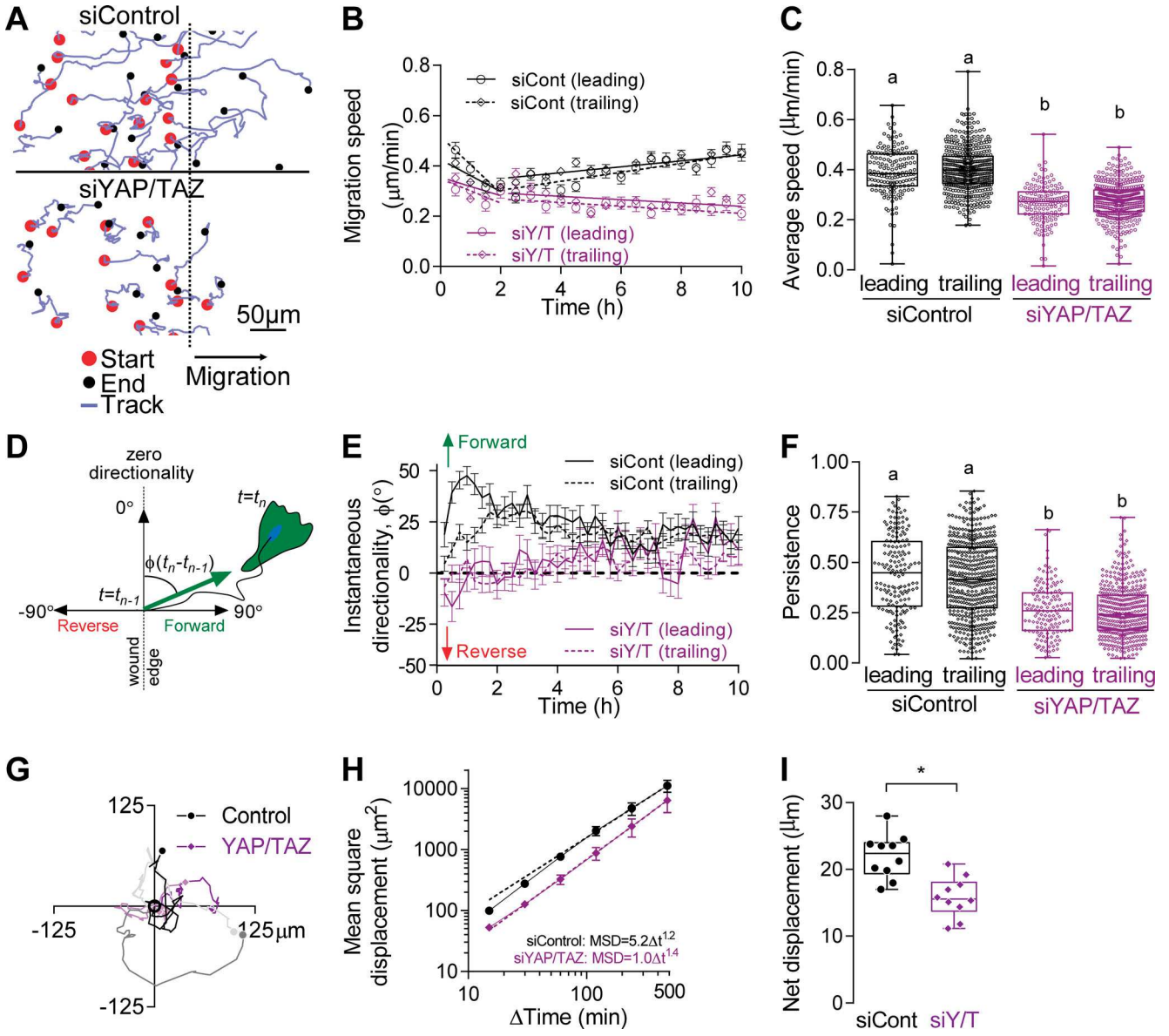

Figure 3. **YAP and TAZ promote collective and individual cell motility.** ECFCs expressing EGFP (siControl) or mTomato (siYAP/TAZ) monolayers were imaged in 15-min intervals over 10 h to track individual cell migration. **(A)** Representative cell migration tracks over 10 h (dashed line indicates starting position). **(B)** Instantaneous average cell migration speed (30 min intervals shown) as a function of time. Cells were grouped into leading (< 100 µm from the front most cell) and trailing (100–500 µm from the front most cell) based on their initial position. n = 140–165 leading cells and n = 437–484 trailing cells. **(C)** Average migration speed per cell over 10 h. $P < 0.0001$; ANOVA with Tukey's post hoc test. **(D)** Schematic of instantaneous cell directionality, defined as the direction, $\varphi(t_n - t_{n-1})$, a cell moved between the current position, t_n, and the previous position, t_{n-1}, relative to the wound edge. **(E)** Instantaneous cell directionality in leading and trailing cells. Data points >0° indicate movement toward the wound, whereas those <0° indicate movement away from the wound. **(F)** Motile persistence, or end-to-end displacement divided by total displacement. $P < 0.0001$; ANOVA with Tukey's post hoc test. **(G)** Random migration of mTomato siYAP/TAZ cells mixed with a 100-fold excess of EGFP siControl cells. **(H)** Mean square displacement of randomly migrating siControl ($R^2 = 0.57$) and siYAP/TAZ ($R^2 = 0.35$) cells. **(I)** Net displacement of randomly migrating cells over 10 h. n = 10; $P < 0.0004$; two-tailed Student's unpaired t test. Repeated significance indicator letters (e.g., a–a) signify $P > 0.05$, while groups with distinct indicators (a vs. b; *) signify $P < 0.05$.

at the trailing edge. To visualize FAs, we immunostained migrating cells for the FA protein, vinculin (Fig. 6 A). YAP/TAZ depletion increased the total number of vinculin$^+$ FA (Fig. 6 B, left), and simultaneously reduced cell area and increasing cell elongation (Fig. 6 B, right; and Fig. S3, A and B).

FAs enlarge and lengthen as they mature (Pasapera et al., 2010). To test the effects of YAP/TAZ depletion on FA maturity, we quantified the number of FAs in 1–10-µm length bins (Fig. 6, C and D). YAP depletion proportionally increased FA number regardless of length, while TAZ and YAP/TAZ depletion shifted the distribution to larger FAs (Fig. 6 D), resulting in increased average FA length (Fig. S3 C). Tyrosine 397 phosphorylated FAK (pFAK) was present in both control and YAP/TAZ-depleted cells, but was localized to the cell periphery in YAP/TAZ-depleted cells (Fig. S3 D).

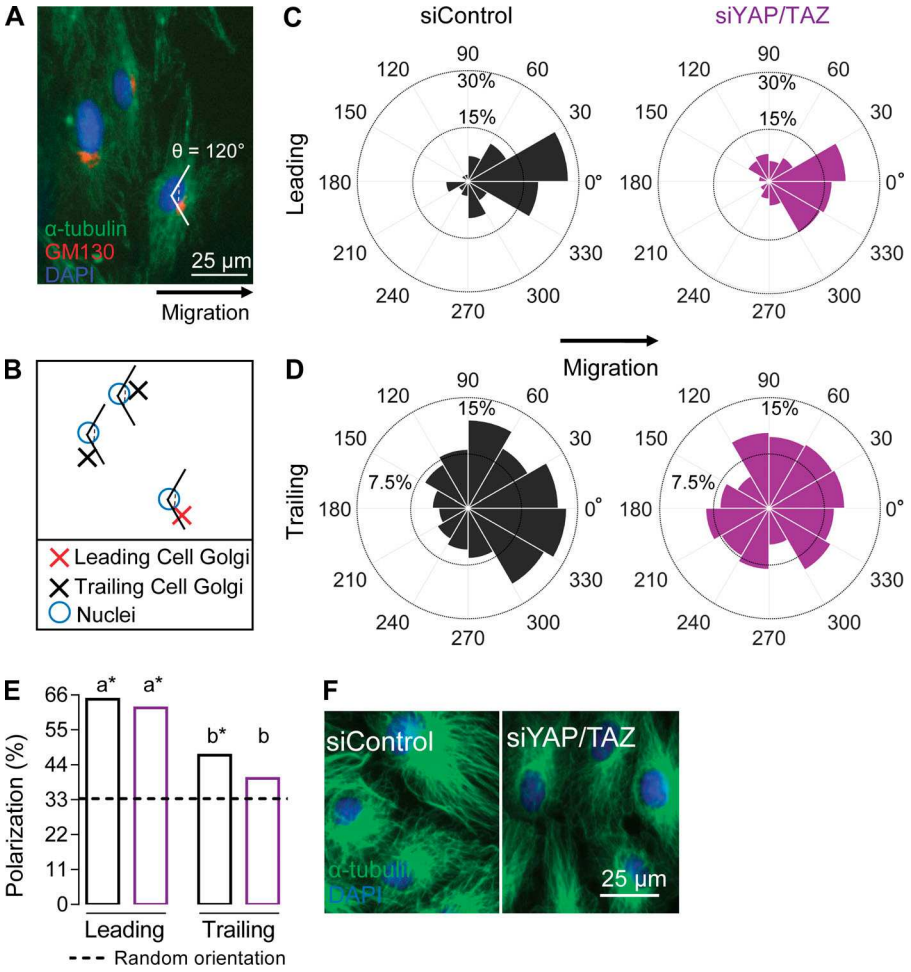

Figure 4. **YAP and TAZ are dispensable for microtubule polarization. (A)** Microtubules (α-tubulin) and Golgi (GM130) were visualized with Alexa Fluor 488 and 594 secondary, respectively. Golgi were considered polarized when within a 120° region centered about a vector extending horizontally from the nuclei (DAPI) in the direction of the wound edge. **(B)** Schematic of Golgi polarization measurement, where blue circles are nuclei, and Xs are Golgi. **(C and D)** Rose plot of Golgi polarization in siControl (black) and siYAP/TAZ (purple) in leading (C) and trailing (D) cells. n = 64–65 leading cells; n = 143–165 trailing cells. **(E)** Percentage of Golgi polarized to the wound in leading and trailing regions; $P < 0.02$; *, $P < 0.002$; χ^2 test with Bonferroni post hoc test. **(F)** α-Tubulin and nuclei visualized by Alexa Fluor 488 secondary and DAPI, respectively. Repeated significance indicator letters (e.g., a–a) signify $P > 0.05$, while groups with distinct indicators (a vs. b) signify $P < 0.05$.

YAP and TAZ regulate FA formation and maturation, but do not inhibit adhesion disassembly

Observation of live cell migration revealed persistent actin-FA connectivity at the cell trailing edge, resulting in protrusion of actin stress fibers beyond the trailing cell membrane, tethering the cell at the trailing edge (Videos 4 and 5), similar to the integrin-bound microaggregates described in keratinocyte migration (Rigort et al., 2004). This led us to ask whether YAP/TAZ could regulate FA disassembly. To test this, we quantified internalization of the proangiogenic (Carlson et al., 2008) integrin β1, using an active β1-integrin antibody internalization assay and evaluated β1 recycling by colocalization with RAB7$^+$ endosomes (Fig. 6 E; Arjonen et al., 2012). YAP/TAZ depletion significantly increased β1-integrin endocytosis (Fig. 6 F), concomitant with increased FA number (compare Fig. 6, A–D). Further, upon internalization, the amount of β1-integrin recycling in RAB7$^+$ endosomes remained constant ($P = 0.69$; Fig. 6 G), suggesting that YAP/TAZ modulate FA formation, but not disassembly or recycling.

YAP and TAZ limit cytoskeletal tension through myosin phosphorylation

Cytoskeletal tension and aggregation of actin filaments into stress fibers is mediated by myosin motor force generation and cross-linking, which stabilize FAs (Oakes et al., 2012). Therefore, we next asked whether YAP and TAZ regulate cytoskeletal remodeling through activation of nonmuscle myosin II. We found that YAP/TAZ depletion increased Serine 19 phosphorylation of myosin light chain (pMYL), which localized to stress fibers, consistent with mechanosensitive recruitment of myosin II to stress fibers (Fig. 6 H; Fernandez-Gonzalez et al., 2009; Luo et al., 2013). Total MYL was unaffected by YAP/TAZ depletion ($P = 0.15$), but percent phosphorylation was significantly increased (Fig. 6, I and J).

We confirmed a functional role for myosin in our model by inhibiting myosin II ADP cycling using Blebbistatin and by inhibiting Rho-associated kinase (ROCK)–mediated phosphorylation of MYL, using Y-27632. Both myosin and ROCK inhibition reduced stress fiber formation and FA maturation in YAP/TAZ-depleted cells (Fig. S3 E). Cytoskeletal tension inhibition had a moderate, but not significant, effect on control cell motility, consistent with other work (Ichida et al., 2011), but substantially increased YAP/TAZ-depleted cell motility, partially rescuing cell migration (Fig. 6 K).

YAP/TAZ regulate NUAK2 to control cytoskeletal tension

These data suggest that YAP/TAZ mediate feedback control of cytoskeletal and FA dynamics through the Rho-ROCK-myosin II pathway. We performed a meta-analysis of previously published chromatin immunoprecipitation sequencing and gene

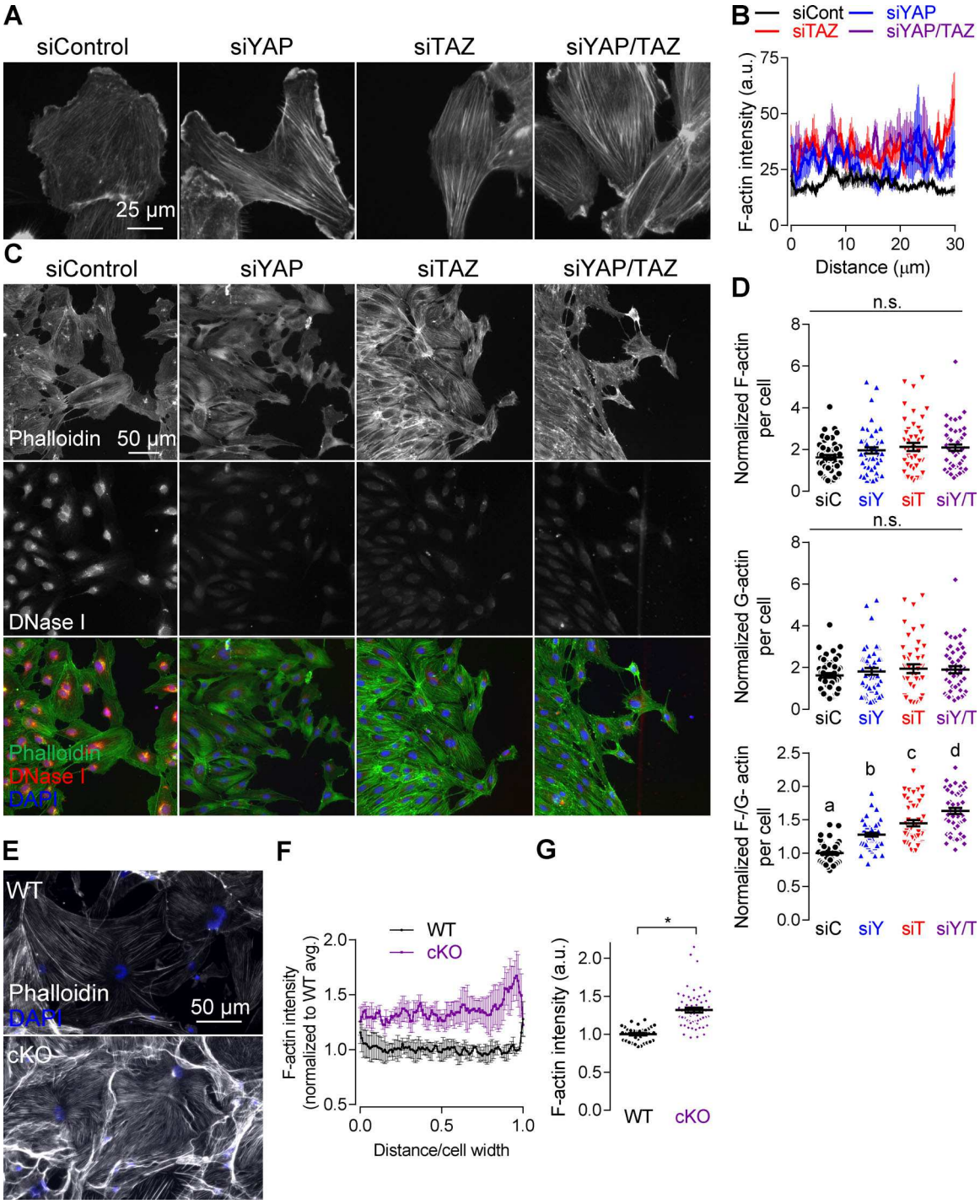

Figure 5. **YAP and TAZ modulate actin polymerization and stress fiber formation. (A)** F-actin, visualized with Alexa Fluor 488 phalloidin. **(B)** Fluorescent intensity line profiles of phalloidin, three cells per condition. **(C)** F- and G-actin visualized by Alexa Fluor 488 and 594 phalloidin and DNase I, respectively. **(D)** F- and G-actin intensity ($P > 0.11$) and F-/G-actin ratio per cell, normalized to siControl; $n = 60$ cells; $P < 0.005$; ANOVA with Tukey's post hoc test. **(E)** WT or *YAP/TAZ* conditional knockout (cKO) BMSCs 14 d after osteoinduction actin visualized with Alexa Fluor 488 phalloidin. **(F)** Actin fluorescent intensity; line scans are the average of three cells per condition, distance normalized to the largest cell in the set. **(G)** Line profile fluorescence. $n = 39–60$ cells; $P < 0.0001$; two-tailed unpaired Student's *t* test. n.s., not significant. Repeated significance indicator letters (e.g., a–a) signify $P > 0.05$, while groups with distinct indicators (a vs. b; *) signify $P < 0.05$.

expression data and identified SNF-like kinase 2 (*NUAK2*), Rho GTPase-activating protein 28 (*ARHGAP28*), and *ARHGAP29* as YAP/TAZ-dependent target genes (Galli et al., 2015; Shen and Stanger, 2015; Lin et al., 2017; Qiao et al., 2017). We confirmed that YAP/TAZ regulate these putative targets by reverse transcription–quantitative PCR (RT-qPCR) of ECFC mRNA. Both *NUAK2* and *ARHGAP28* were significantly increased after YAP/TAZ depletion, but *ARHGAP29* was significantly reduced (Fig. 7

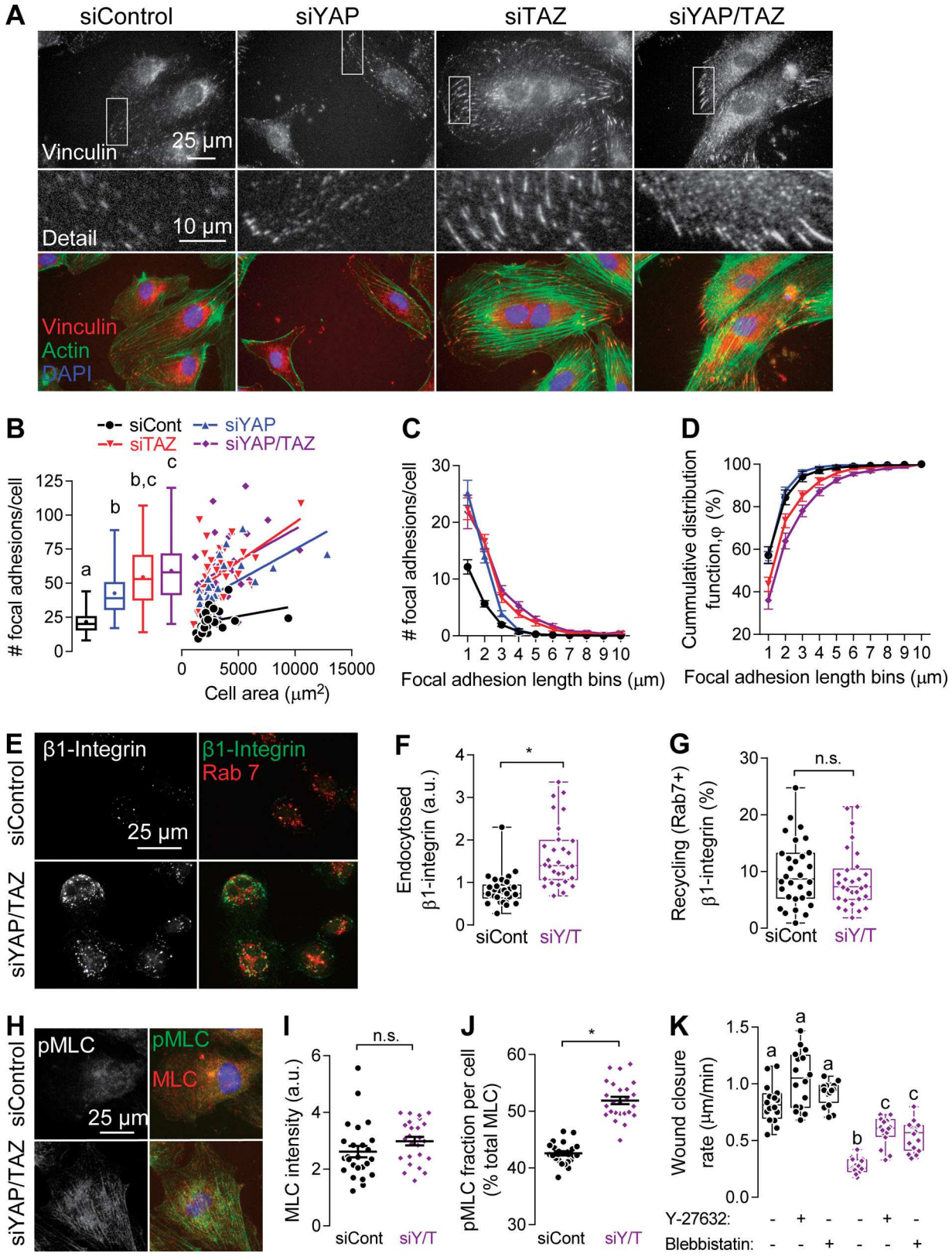

Figure 6. **YAP and TAZ modulate FA remodeling, but not integrin β1 recycling, through myosin. (A)** Vinculin and F-actin, visualized with Alexa Fluor 594 secondary and 488 phalloidin, respectively. **(B)** Average number of FAs per cell as a function of cell area. n = 30–34; $P < 0.004$; ANOVA with Tukey's post hoc test. **(C and D)** FA size histogram (C) and cumulative distribution function (D) or the percentage of FAs in a cell of a given size. **(E)** β1-integrin internalization and recycling. Live ECFCs were incubated with antibodies targeting active β1-integrin (10 μg/ml), which were endocytosed for 45 min, followed by acid wash and fixation. Internalized integrin was detected with Alexa Fluor 488 secondary. RAB7⁺ endosomes were visualized with Alexa Fluor 594 secondary. **(F)** Total

fluorescent intensity of endocytosed β1-integrin. $n = 30$; $P < 0.0001$; two-tailed Student's unpaired t test. **(G)** Fluorescent intensity of recycling endocytosed β1-integrin colocalized with RAB7$^+$ endosomes. **(H)** MLC and pMLC visualized by Alexa Fluor 594 and 488 secondaries, respectively. **(I)** Total MLC intensity per cell. $n = 25$; $P > 0.15$; two-tailed unpaired Student's t test. **(J)** Percentage of MLC phosphorylated at Ser19 (i.e., pMLC/total MLC intensity × 100, per cell). $n = 25$; $P < 0.0001$; two-tailed Student's unpaired t test. **(K)** Wound closure rates after treatment with Y-27632 (10 µM) or Blebbistatin (20 µM). $n = 16$; $P < 0.0001$; ANOVA with Tukey's post hoc test. n.s., not significant. Repeated significance indicator letters (e.g., a–a) signify $P > 0.05$, while groups with distinct indicators (a vs. b; *) signify $P < 0.05$.

A). Notably, NUAK2 was up-regulated sevenfold in YAP/TAZ-depleted cells. NUAK2 expression is induced by cytoskeletal tension to phosphorylate and sequester the myosin-binding subunit (MYPT1) of MLCP, preventing dephosphorylation of myosin II (Zagórska et al., 2010; Vallenius et al., 2011). Therefore, we chose to orthogonally probe the function of myosin II phosphorylation by perturbing NUAK2 expression.

To better understand the kinetics of YAP/TAZ-dependent gene induction, we examined gene expression at 0, 1, and 12 h after initiation of migration. As expected, YAP/TAZ depletion abrogated inducible expression of the canonical YAP/TAZ-TEAD target genes, *Cyr61* (Fig. 7 B), but also significantly up-regulated *NUAK2* at 1 h (Fig. 7 B), consistent with increased myosin phosphorylation (compare Fig. 6). We hypothesized that normalization of NUAK2 expression in YAP/TAZ-depleted cells would partially restore cytoskeletal equilibrium. To test this hypothesis, we delivered siRNA targeting *YAP*, *TAZ*, and *NUAK2*, where we expected that NUAK2 codepletion with YAP/TAZ to normalize NUAK2 expression. Triple depletion of YAP/TAZ/NUAK2 did not affect *YAP* or *TAZ* knockdown efficiency at the mRNA level (Fig. S4, E and F) or TAZ at the protein level (Fig. S4, H and I), but normalized *NUAK2* mRNA expression (Fig. S4 G).

NUAK2 codepletion with YAP/TAZ had a significant impact on cytoskeletal morphology, most notably by reducing stress fiber fluorescent intensity in YAP/TAZ-depleted cells (Fig. 7, D and C). NUAK2 depletion did not alter F- or G-actin intensity or ratio (Fig. 7 E), but rescued the increase in actin polymerization caused by YAP/TAZ depletion, measured by immunofluorescence (Fig. 7 E). However, actin polymerization, measured by F- and G-actin fractionation, was only moderately increased ($P = 0.08$; Fig. 7, F and G). We orthogonally validated these results by treating YAP/TAZ-depleted cells with WZ4003, a selective inhibitor of NUAK1/2 (Banerjee et al., 2014; Fig. S4A). WZ4003 treatment significantly F- and G-actin fluorescence ratio in YAP/TAZ-depleted cells (Fig. S4, A and B). These data suggest that YAP- and TAZ-regulated cytoskeletal tension and stress fiber formation through NUAK2, but have a limited effect on actin polymerization per se.

YAP and TAZ spatially control vinculin incorporation into structural FAs via NUAK2

Together, these data implicate YAP and TAZ in feedback control of actomyosin tension through Rho-ROCK-myosin II to prevent cellular tethering at FAs. To evaluate this feedback in structural FAs, we removed poorly adherent FAs by detergent solubilization, leaving the structural fraction (Yamashita et al., 2014). The composition of the structural FA was determined by immunostaining for vinculin incorporation into FAs in single cells (Fig. 8 A). YAP/TAZ depletion increased the amount of structural vinculin (Fig. 8 A). FA size was increased by YAP/TAZ depletion, but NUAK2 codepletion significantly rescued vinculin$^+$ FA size (Fig. 8 C).

FA remodeling and cell-generated traction is spatially controlled and occurs predominantly at leading and trailing edges (Reinhart-King et al., 2003; Totsukawa et al., 2004). Further, in YAP/TAZ-depleted cells, we observed preferential FA maturation at the cell periphery. Therefore, we subdivided FAs in each cell into peripheral (5 µm from every edge) or central regions (Fig. 8 B). YAP/TAZ and YAP/TAZ/NUAK2 depletion had no effect on FA number or morphology within the central region of interest (Fig. 8 C); however, peripheral FA length was significantly reduced by NUAK2 codepletion (Fig. 8 C). We further confirmed these observations using the NUAK1/2 inhibitor WZ4003, which normalized FA morphology in YAP/TAZ-depleted cells (Fig. S4 C). Interestingly, WZ4003 compromised vinculin incorporation into FAs, more so than NUAK2 depletion or WZ4003 treatment in control cells.

YAP/TAZ modulate myosin tension to enable FA polarization

YAP/TAZ depletion impaired persistent and directional cell migration, but not MTOC polarization or initial direction sensation. Persistent motility requires that FAs preferentially form at the leading edge, mature in the lamellum, and disengage at the trailing edge (Reinhart-King et al., 2003; Gupton and Waterman-Storer, 2006). To test this, we quantified FA polarization as the distance between the centroid of the nucleus and the centroid of structural FAs (Fig. 8 D). YAP/TAZ depletion significantly reduced FA polarization, which were restored by codepletion of NUAK2 (Fig. 8 E). NUAK2 codepletion partially rescued YAP/TAZ-dependent anchorage release and migration (Fig. 8 F), but WZ4003 treatment did not (Fig. S4 D).

YAP/TAZ regulate Serine phosphorylation status of myosin phosphatase

We found that YAP/TAZ depletion increased expression of NUAK2, which has been shown to regulate Serine phosphorylation of myosin phosphatase (MYPT1, or PPP1R12A) at Ser 445, 472, and 910 (Yamamoto et al., 2008; Zagórska et al., 2010). Antibodies to these sites were unavailable, so to test whether YAP/TAZ regulate MYPT1 Serine phosphorylation, we next immunoprecipitated MYPT1 and immunoblotted against total phospho-Serine (Fig. 8, G and H). YAP/TAZ depletion enhanced MYPT1 Serine phosphorylation, but this was not rescued by NUAK2 depletion (Fig. 8 H). There are nine Serine residues in the human MYPT1 protein that have been shown to have a direct effect on MYPT1 function (Chen et al., 2015). Should NUAK2 only regulate MYPT1 phosphorylation at Ser 445, 472, and 910 (Yamamoto et al., 2008; Zagórska et al., 2010), these changes may be masked by other phosphorylation sites also marked by the general p-Serine antibody.

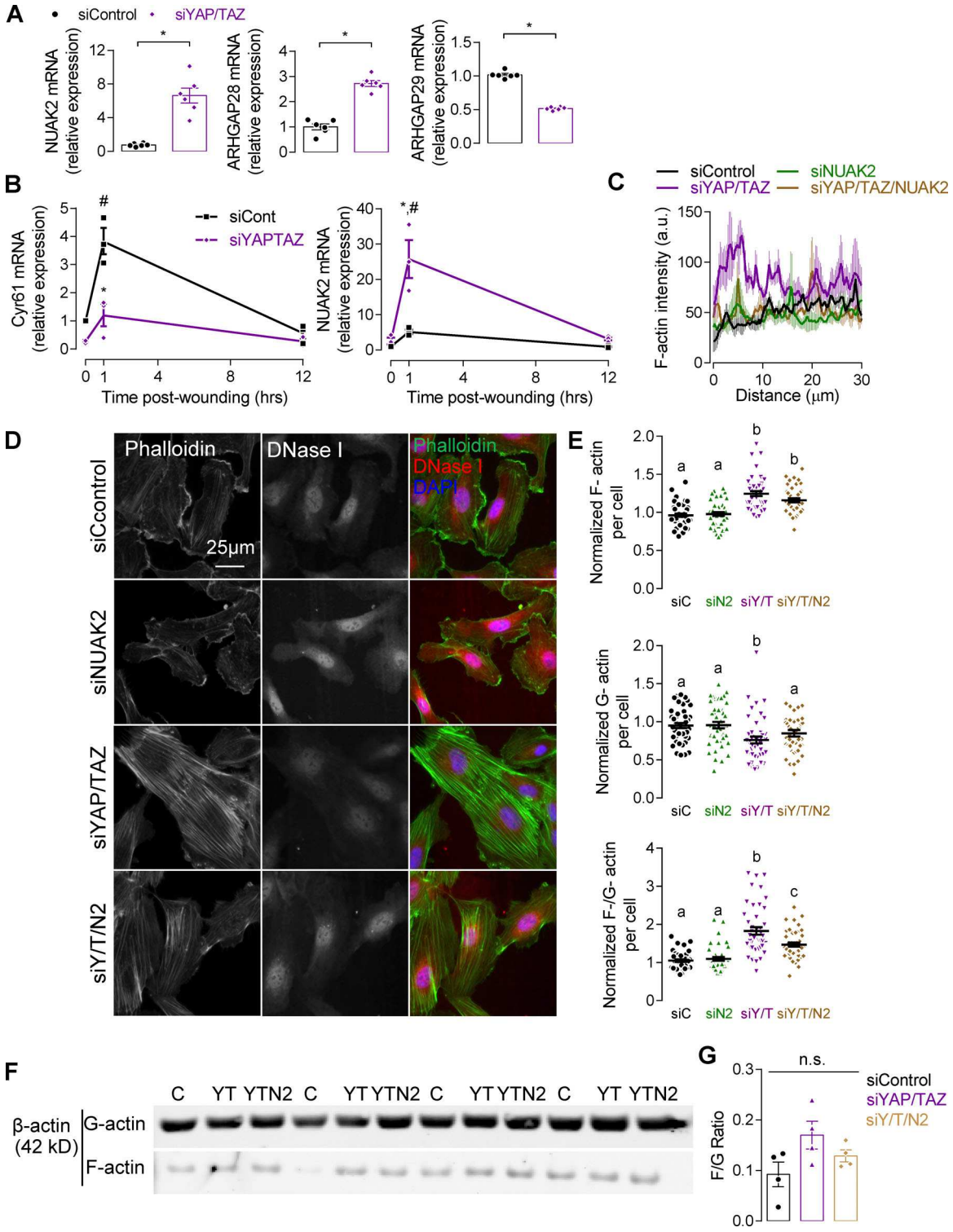

Figure 7. **YAP and TAZ modulate actin polymerization through NUAK2 regulation**. **(A)** ECFCs were screened for YAP/TAZ-regulated cytoskeletal regulators *NUAK2*, *ARHGAP28*, and *ARHGAP29*; $n = 6$; *, $P < 0.0001$, two-tailed Student's unpaired *t* test. **(B)** *Cyr61* and *NUAK2* expression in migrating ECFCs. $n = 3$; *, $P < 0.0004$ versus control at 1 h; #, $P < 0.0001$ versus 0 h, two-way ANOVA with Tukey's post hoc test. **(C)** Fluorescent intensity line profiles of phalloidin, three cells per condition. **(D)** F- and G-actin visualized with Alexa Fluor 488 secondary and 594 phalloidin. **(E)** F-actin ($P < 0.0001$) and G-actin intensity ($P < 0.007$) and F-/G-actin ratio per cell, normalized to siControl. $n = 60$ cells; $P < 0.005$; ANOVA with Tukey's post hoc test. **(F)** Western blot of β-actin in F- and G-fractions of ECFC lysate **(G)** F-/G-actin ratio of β-actin densitometry measurements in F- and G-fractions. $n = 4$ samples; $P > 0.08$; ANOVA with Tukey's post hoc test. n.s., not significant. Repeated significance indicator letters (e.g., a–a) signify $P > 0.05$, while groups with distinct indicators (a vs. b) signify $P < 0.05$.

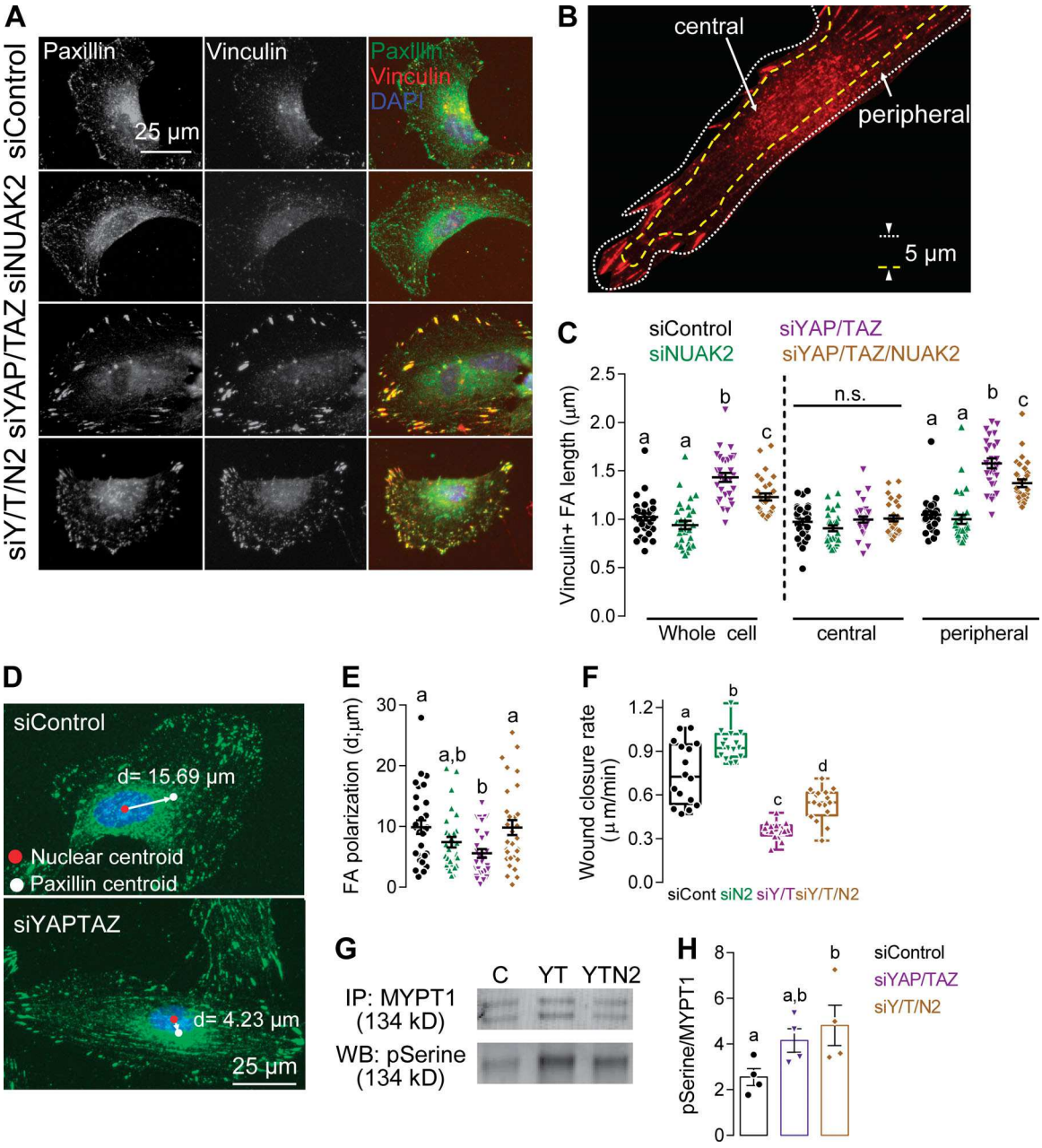

Figure 8. **YAP/TAZ-regulated NUAK2 enhances FA maturation and polarization, resulting in reduced cell motility.** ECFCs were Triton-extracted concurrent with fixation for immunofluorescence of structural FAs. **(A)** Representative images of vinculin and paxillin visualized with Alexa Fluor 594 and 488 secondary, respectively. **(B)** Spatial differences in FA morphology were detected by subdividing cells into peripheral and central (5 μm from the edge of the cell) regions. FA length, an indicator of maturation, was found at the center and periphery of individual cells. **(C)** Vinculin⁺ FA length in the whole cell ($P < 0.003$), central region ($P > 0.1$), and peripheral region ($P < 0.006$), ANOVA with Tukey's post hoc test for the whole cell and center and Kruskal-Wallis with Dunn's post hoc test for the periphery. **(D)** Representative FA polarization distance indicated by the white line between the nucleus (red dot) and FA (white dot) intensity centroid. **(E)** FA polarization distance. $P < 0.02$; ANOVA with Tukey's post hoc test. **(F)** ECFC wound closure rate after NUAK2 codepletion; $n = 16$; $P < 0.006$; ANOVA with Tukey's post hoc test. **(G)** Immunoprecipitated MYPT1 (top), immunoblotted against total phosphorylated Serine (bottom), representative blot of $n = 4$ shown. **(H)** Quantification of p-Ser MYPT1/MYPT1; $n = 4$; $P < 0.04$; ANOVA with Tukey's post hoc test. n.s., not significant. Repeated significance indicator letters (e.g., a–a) signify $P > 0.05$, while groups with distinct indicators (a vs. b) signify $P < 0.05$.

YAP and TAZ are essential for endothelial vacuole formation, tubulogenesis, and sprouting angiogenesis

ECFC vacuole formation is sensitive to 3D matrix mechanical properties (Bailey et al., 2011). We cultured ECFCs in oligomeric collagen matrices containing native cross-links conducive to vacuole formation in vitro and in vivo (Bailey et al., 2011; Whittington et al., 2013). YAP and TAZ depletion completely abrogated 3D vacuolation and interconnected vasculogenic network formation in oligomeric collagen matrices (G' = 132 Pa; Fig. 9 A). Similarly, in the matrigel tubulogenesis assay, YAP and/or TAZ depletion combinatorially reduced tubular network length and number (Fig. 9, B and C), with a greater effect of TAZ

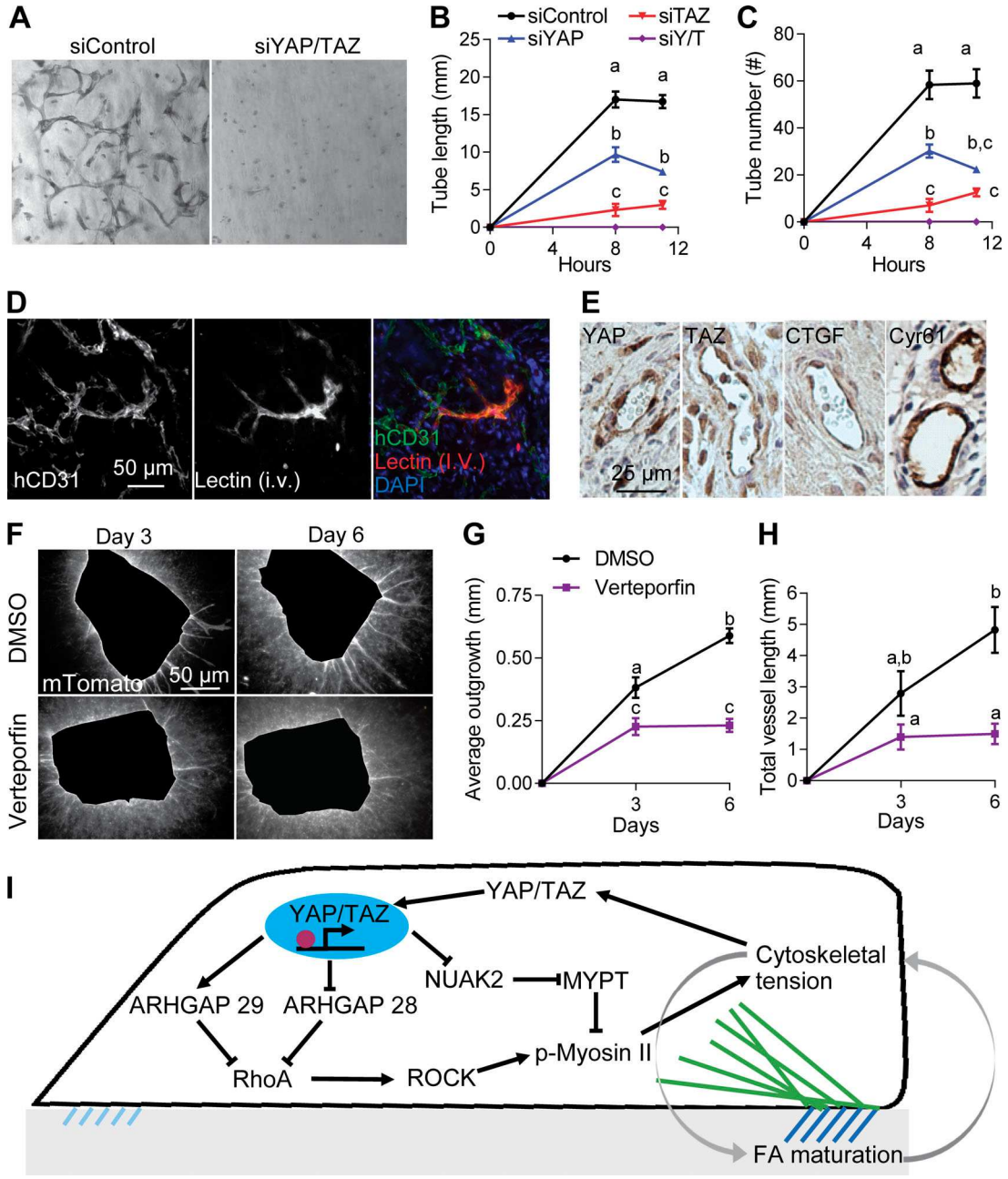

Figure 9. **YAP and TAZ mediate endothelial tubulogenesis, vacuolation, and sprouting angiogenesis. (A)** Phase contrast images of 3D ECFC vasculogenesis in oligomeric collagen matrices (G′ = 132 Pa). **(B and C)** ECFC tubulogenesis on Matrigel: tube length ($P < 0.0032$; B) and number ($P < 0.0003$; C). $n = 12$; two-way ANOVA with Tukey's post hoc test. **(D and E)** ECFC-embedded oligomeric matrices recovered from NOD-scid mice. **(D)** Functioning vasculature and human endothelium visualized using Rhodamine lectin and Alexa Fluor 647 anti-human CD31, respectively. **(E)** Chromogenic HRP substrate DAB (brown) was used to visualize YAP, TAZ, CTGF, and CYR61. **(F–H)** Whole mTomato-expressing aortas were extracted, segmented, and embedded in collagen for the aortic sprout assay. **(F)** mTomato-expressing cell outgrowth from aortic explants. **(G)** Cell outgrowth, average distance from the explant edge. $n = 17–21$ rings; $P < 0.001$; two-way ANOVA with Tukey's post hoc test. **(H)** The sum of vascular sprout lengths from explants. $P < 0.03$; two-way ANOVA with Tukey's post hoc test. **(I)** Schematic of the transcriptional negative feedback loop that regulates intracellular tension. Cytoskeletal tension is increased by ROCK activation of myosin II causing YAP and TAZ nuclear localization. Active YAP and TAZ inhibit ROCK-mediated MLC phosphorylation by transcriptional control of NUAK2 and ARHGAP 28 and 29 expression, preventing overactivation of myosin II. Repeated significance indicator letters (e.g., a–a) signify $P > 0.05$, while groups with distinct indicators (a vs. b) signify $P < 0.05$.

versus YAP depletion, consistent with their effects on cytoskeletal dynamics.

ECFCs have potential as an autologous or allogeneic cell source for vasculogenic therapies (Ingram et al., 2004, 2005). To evaluate YAP/TAZ activation during transplanted ECFC vasculogenesis in vivo, we implanted human ECFC-laden collagen matrices in the subcutaneous space of NOD-scid mice. Establishment of a functional human neovascular plexus that inosculated with the host vasculature was demonstrated by confocal reconstruction of human CD31⁺ vessels that costained

with intravenously perfused Rhodamine-labeled UEA-I lectin (Fig. 9 D). Immunostained human neovasculature revealed nuclear YAP/TAZ and robust expression of target genes CTGF and Cyr61 in vivo (Fig. 9 E).

Finally, we evaluated the transcriptional role of YAP and TAZ in angiogenic sprouting ex vivo using verteporfin (VP), a selective inhibitor of the YAP/TAZ-TEAD transcriptional complex (Liu-Chittenden et al., 2012). Treating ECFCs with 2 µM VP reduced YAP and TAZ expression as well as the canonical target genes *CTGF*, *Cyr61*, and *SERPINE1*, consistent with the effects of YAP and/or TAZ (siRNA; Fig. S5 A). However, contrary to YAP and TAZ depletion, VP significantly reduced *NUAK2* expression (siRNA; Fig. S5 A). Regardless, VP treatment reproduced the cytoskeletal and FA defects caused by RNAi depletion of YAP/TAZ (Fig. S5, B–D). Like YAP/TAZ siRNA, VP treatment had no effect on F- or G-actin intensity ($P > 0.11$), but increased the ratio of F- and G-actin fluorescent intensities (Fig. S5 C).

To evaluate YAP/TAZ function during sprouting angiogenesis ex vivo, we quantified vessel outgrowth in the aortic sprout assay. VP treatment of vessel explants significantly reduced nonvessel cellular outgrowth, a measure of 3D cell migration (Fig. 9, F and G) and reduced neovessel length (Fig. 9 H).

Discussion

Whether existing proteins are sufficient to maintain migration, independent of transcription, is a matter of debate (Weiss and Chang, 1973; Chen et al., 1994). Here, we show that de novo gene transcription is essential for persistent ECFC motility and identify the transcriptional coactivators YAP and TAZ as regulators of migration through cell-intrinsic feedback control of Rho-ROCK-myosin II activity, partially through transcriptional repression of the MLCP regulator NUAK2 (Fig. 9 I). We validated the role of the Rho-ROCK-YAP/TAZ-NUAK2 signaling axis using RNAi and pharmacological inhibitors. Depletion or inhibition of MLCP regulatory kinase NUAK2 as well as myosin II/ROCK inhibition partially restored cell motility by relieving cytoskeletal tension. Notably, YAP/TAZ depletion, YAP/TAZ-TEAD inhibition, and global transcriptional/translational inhibition consistently increased stress fiber and FA maturation and arrested cell motility. Together, these data demonstrate that cytoskeletal dynamics, initiated by cell migration, activate YAP and TAZ to drive a transcriptional regulation program that feeds back to modulate cell mechanics, maintain a responsive cytoskeletal equilibrium, and prevent migration arrest.

Cells require new gene expression to replace consumed or degraded proteins. However, we found that transcription inhibition causes eventual motility arrest, not due to depletion of the components of the molecular clutch, but rather through dysregulated cytoskeletal tension and FA maturation. This is consistent with the reported stability of the molecular clutch proteins. For example, vinculin and talin have a half-life of 18–21 h (Lee and Otto, 1996), and β-actin has a half-life of 48 h (Antecol et al., 1986), while myosin contractile motors in muscle are stable for days (Martin et al., 1977). Consistent with this, stress fiber and FA formation continued during long-term transcription inhibition. Further, myosin tension generation and FA reinforcement occurs more rapidly than de novo protein synthesis (Polte et al., 2004; Elosegui-Artola et al., 2016). However, immediate early genes are transcriptionally up-regulated during migration and enhance cell motility (O'Brien et al., 1990; Ryseck et al., 1991; Pepper et al., 1992). These observations led us to explore the transcriptional mechanisms that modulate cytoskeletal remodeling to enable persistent motility.

We found that YAP/TAZ mediated transcription-moderated cytoskeletal mechanics, and YAP/TAZ depletion or inhibition phenocopied global transcription inhibition. Thus, we conclude that YAP and TAZ act to dissipate cytoskeletal tension in part through a cell-intrinsic feedback mechanism dependent on NUAK2 control of myosin II activation. Some recent reports implicate YAP in feed-forward promotion of cytoskeletal tension (Lin et al., 2017; Nardone et al., 2017), potentially through outside-in feedback through regulation of extracellular matrix (ECM) production and subsequent mechanosensation (Calvo et al., 2013; Liu et al., 2015; Porazinski et al., 2015). In contrast, our data are consistent with evidence from cells that do not produce extensive ECM, implicating YAP/TAZ-mediated ARHGAP expression in suppression of actin polymerization and cytoskeletal tension (Qiao et al., 2017). While it is clear that the functions and relative roles of YAP and/or TAZ are cell type– and context-dependent, synthesizing available data, we conclude that YAP/TAZ mediate both cell-autonomous and outside-in feedback systems to modulate cell and tissue tension.

Here, we identify a cell-autonomous feedback pathway by which YAP/TAZ suppress cytoskeletal tension by regulating myosin II, verified through orthogonal mechanical and biochemical measurements. We further validated this negative feedback system through both loss-of-function and rescue experiments featuring pharmacologic, RNAi, and conditional deletion-based approaches, and we identify the YAP/TAZ-TEAD–dependent target gene, NUAK2, as a novel negative regulator of cell migration through cytoskeletal tension in ECFCs. We identify YAP/TAZ-mediated repression of NUAK2 as a key modulator of cytoskeletal tension. These data both conflict and conform to previously published literature (Lin et al., 2017; Qiao et al., 2017), but support the common hypothesis that YAP and TAZ can act both as coactivators and corepressors of gene expression, depending on cell type and environment (Kim et al., 2015; Otsubo et al., 2017; Goto et al., 2018). While YAP/TAZ depletion largely recapitulates the effects of global transcription inhibition, other mechanotransductive factors may contribute to parallel or interacting feedback loops. For example, the transcriptional coactivator MRTF transactivates serum response factor–dependent gene expression, including actomyosin genes, MLC2 and β-actin, and FA components talin, vinculin, and zyxin (Medjkane et al., 2009; Esnault et al., 2014). Similarly, AP-1 transcribes cytoskeletal regulator gelsolin-like capping protein while down-regulating fibronectin (Ozanne et al., 2007). Interestingly, there is significant overlap between MRTF, AP1, and TEAD occupancy at inducible genes (Enzo et al., 2015; Kim et al., 2017b). Thus, transcriptional mechanotransductive mechanisms may be interdependent, and further study will be required to clarify how complex multitranscription factor dynamics tune the cytoskeleton to regulate motility and mechanosensation.

YAP and TAZ can have either convergent or divergent functions depending on context. Global deletion of *YAP* is embryonic lethal, due to impaired vasculogenesis, whereas *TAZ* knockout mice survive birth, but only 50–65% reach adulthood due to polycystic kidney disease (Hossain et al., 2007). In vivo evidence from our group and others have found that YAP versus TAZ functional redundancy is cell type specific. For example, YAP is essential, but TAZ is dispensable, during cardiac development (Xin et al., 2013), while YAP and TAZ are combinatorial in bone development (Kegelman et al., 2018). Interestingly, we observe a greater effect of TAZ ablation in ECFCs. These data are consistent with recent descriptions of the roles of YAP and TAZ in endothelial cell migration and vascular integrity (Neto et al., 2018). However, others have observed an increase in HUVEC migration when YAP is restricted to the cytosol, in implicating a cytosolic YAP–CDC42 signaling axis, though the mechanism remains unclear (Sakabe et al., 2017). Consistent with this, we found that selective inhibition of YAP/TAZ-TEAD interaction with VP increased cytoskeletal tension, but not through overexpression of NUAK2, suggesting either additional transcriptional targets or potentially complementary, cytosolic roles for YAP and TAZ. While further research will be necessary to dissect potentially distinct coeffector interactions or transcriptional targets of YAP and TAZ, these data contribute to the emerging evidence of crosstalk between transcriptional activity and cytoskeletal dynamics.

This study provides new mechanistic understanding to explain recent observations regarding the roles of YAP and TAZ in retinal angiogenesis, liver vascularization, and hindbrain hemorrhage (Sakabe et al., 2017). Prior data implicates defects in proliferation (Shen and Stanger, 2015), tip cell sprouting (Choi et al., 2015; Sakabe et al., 2017; Wang et al., 2017), and vascular integrity (Kim et al., 2017a). Our findings establish a new YAP/TAZ-Rho-ROCK-myosin II feedback axis as a critical mechanism for neovascular function and points to transcriptional-cytoskeletal feedback as a key regulator of cell motility.

Materials and methods

Cell culture and transfection

ECFCs were cultured as previously described (Ingram et al., 2004, 2005). In brief, ECFCs were seeded on collagen (5 µg/cm^2)-coated tissue culture polystyrene and maintained at 37°C and 5% CO_2 in endothelial growth medium (EGM-2 with bullet kit; Lonza; CC-3162) supplemented with 1% penicillin/streptomycin (Corning) and 10% defined fetal bovine serum (Thermo Fisher), referred to as full medium. ECFCs were released from culture dishes using TrypLE Express (Gibco) and used between passages six and eight.

Murine BMSC isolation and differentiation

Mouse BMSCs were isolated from either WT or Osterix-conditional *YAP/TAZ* knockout mice and cultured at 37°C and 5% O_2 in medium supplemented with 10 ng/ml fibroblast growth factor (FGF-2; Rodda and McMahon, 2006; Caroti et al., 2017; Kegelman et al., 2018). In brief, mice were anesthetized by isoflurane inhalation (2%) and euthanized via cervical dislocation. Long-bone samples were dissected, and marrow cavities were flushed out into a tissue culture plastic flask for 3–5 d. BMSCs were initially isolated and cultured at 5% O_2 in RPMI1640 with 20% fetal bovine serum (Sigma), 10 ng/ml basic FGF (Austral Biologicals), 1% penicillin-streptomycin, and 1 mg/ml doxycycline. After P1, BMSCs were cultured at 5% O2 in DMEM expansion media with 20% fetal bovine serum, 10 ng/ml basic FGF, 1% penicillin-streptomycin, and 1 mg/ml doxycycline. BMSCs were then seeded at 21% O_2 into 6-well plates (9,000 cells/cm^2) and allowed to adhere for 24 h before being switched to osteogenic induction medium, composed of DMEM, 10 mM β-glycerophosphate, 100 nM dexamethasone, 50 µM ascorbic acid, 10% fetal bovine serum, and 1% penicillin-streptomycin, without doxycycline or FGF-2. The osteogenic medium was changed every other day before fixation for immunofluorescent staining.

ECFCs were depleted of YAP and TAZ using siRNA-loaded lipofectamine RNAimax (Invitrogen) according to the manufacturer's instructions. In brief, ECFCs were seeded on collagen-coated, 6-well plates, 10^5 cells per well, in antibiotic-free medium and kept in culture for 24 h followed by transfection at ∼50% confluence. Transfection was performed using a final concentration 0.3% (vol/vol) lipofectamine RNAimax with 15 pM RNAi duplexes (custom oligonucleotides; Dharmacon) per well. Transfected ECFCs were used 24–48 h after transfection.

ON-TARGET plus nontargeting siRNA and SMARTpool NUAK2 siRNA (L-005374-00-0005) were obtained from Dharamacon. Custom siRNA were created based on sequences previously described (Dupont et al., 2011): YAP 1, sense, 5′-GACAUC UUCUGGUCAGAGA-3′, and YAP 1, anti-sense, 5′-UCUCUGACC AGAAGAUGUC-3′; YAP 2, sense, 5′-CUGGUCAGAGAUACUUCU U-3′, and YAP 2, anti-sense, 5′-AAGAAGUAUCUCUGACCAG-3′; TAZ 1, sense, 5′-ACGUUGACUUAGGAACUUU-3′, and TAZ 1, anti-sense, 5′-AAAGUUCCUAAGUCAACGU-3′; TAZ 2, sense, 5′-AGGUACUUCCUCAAUCACA-3′, and TAZ 2, anti-sense, 5′-UGU GAUUGAGGAAGUACCU-3′.

Collagen synthesis and characterization

Collagen oligomers and monomers were synthesized and polymerized as previously described (Kreger et al., 2010; Bailey et al., 2011; Whittington et al., 2013). In brief, porcine skin collagen was isolated using acetic acid extraction, yielding a viscous collagen composition containing both oligomeric and monomeric collagen (Critser et al., 2010). Monomeric collagen was purified by salt precipitation, selectively removing oligomeric collagen from the solution (Whittington et al., 2013).

Collagen mechanical properties were defined as previously described (Kreger et al., 2010). Storage and loss moduli were measured in oscillatory and shear and compression on a stress controlled AR2000 Rheometer (TA instruments). Collagen samples were polymerized in situ at 37°C for 30 min and then tested with a shear strain sweep from 0.01 to 5% at 1 Hz. Following the strain sweep compressive modulus (E_c) was measured in unconfined compression at a strain rate 20 µm/s (2.76% strain per second). Stress was calculated as the normal force divided by plate area (12.57 cm^2). E_c was then calculated as the slope of the stress strain curve.

Animal handling

All animal experiments were approved by the Institutional Animal Care and Use Committee at the University of Notre Dame and Indiana University School of Medicine.

10^6 cord blood–derived ECFCs were resuspended in 250 µl collagen gel (G' = 200 Pa; Geniphys; Standarized Oligomer Polymerization kit) plus 10% human platelet lysate (Cook) on ice and then polymerized for 30 min at 37°C in a well of 48-well plate. Matrices were covered with 500 µl culture medium until transplantation. Cellularized matrices were transplanted into the abdominal flanks of 6–12-wk-old NOD-scid immunodeficient mice, anesthetized by inhaled isoflurane under aseptic conditions. After 14 d, 100 µl of Rhodamine-labeled *Ulex europaeus* Agglutinin I (UEA I; referred to in this paper as lectin; Vector Laboratories) were intravenously injected into the transplanted mice 30 min before the mice were euthanized. The grafts were collected from the mice and fixed in 4% paraformaldehyde at 4°C overnight and prepared for immunofluorescence or paraffin embedding.

Whole mouse aortas were extracted as previously described (Baker et al., 2012). In brief, 4–6-wk-old C57BL/6 mice with or without the mTomato/mGFP (*mTmG*) transgene were anesthetized by inhalation of 5% isoflurane in oxygen, followed by physical euthanasia by bilateral thoracotomy. Whole aortas from the aortic arch to the abdominal insertion were extracted and cleaned of fat and branching vessels and then flushed with dPBS containing 10 U/ml of heparin sodium (Hospira). Aortas were sectioned into 0.5-mm rings and serum starved overnight in EBM-2 with 1% penicillin/streptomycin. Aortic rings were encapsulated in oligomeric collagen (G' = 132 Pa) in 96-well plates with full medium containing either VP (Sigma) or an equal volume of DMSO (Sigma). Fluorescent z stacks of aortic rings expressing mTmG were taken with a Leica DMi8, 0, 3, and 6 d after polymerization. Sprouting aortas not expressing mTomato were fixed with 4% paraformaldehyde for immunofluorescence.

PA hydrogels

PA hydrogels were prepared as previously described (Damljanović et al., 2005) with slight modifications. In brief, 24 × 50-mm no. 1 glass coverslips were washed with soap and water and rinsed in ethanol. Coverslips were functionalized using 0.5% (vol/vol) 3-(Trimethoxysilyl)propyl methacrylate (Sigma) in ethanol. Coverslips were cut to 24 × 20-mm sections to fit in 6-well plates. PA precursor solutions were prepared from 40% acrylamide (EMD Millipore), 2% Bis-acrylamide (Amresco), tetramethylethylenediamine (Thermo Fisher), and ammonium persulfate (Amresco). 45 µl of PA precursor solution was pipetted on to hydrophobic glass slide and topped with the functionalized glass coverslips and allowed to polymerize for 30 min.

Hydrogels were functionalized with ECM using techniques described previously (Damljanović et al., 2005). Hydrogels were first treated with hydrazine hydrate (Sigma) overnight then washed with deionized water followed by 1 h in 5% (vol/vol) acetic acid then 1 h in deionized water. Collagen (MP Biomedicals) in 50 mM sodium acetate buffer (pH 4.5; Sigma) with 4 mg/ml sodium (meta)periodate (Sigma) for half an hour in the dark. ECM was then applied to the hydrazine hydrate functionalized hydrogels for 1 h. Hydrogels were thoroughly washed in deionized water and equilibrated in PBS overnight. Hydrogels were sterilized for 15 min under a germicidal UV lamp and then washed in EBM-2 and equilibrated in full medium for at least 8 h. For immunofluorescence experiments, 8.5 × 10^3 cells per cm^2 were seeded per hydrogel.

Migration assays

Migration assays were performed on confluent layers of transfected and/or inhibitor-treated cells. 24 h after transfection cells were washed twice in endothelial basal medium (EBM-2) and then serum starved in EBM-2 for 2 h. The collective migration wounding assay was performed as described previously (Boerckel et al., 2014). Migration was initiated by scratching monolayers were vertically and horizontally with the tip of a 200-µl pipette tip, followed by two washes in EBM-2 and addition of full medium. Actinomycin D (Sigma), puromycin (Sigma), WZ4003 (MedChem Express), Y-27632 (Tocris), and Blebbistatin (Sigma) were added into basal medium, 1 h after starting serum starvation and in full medium after initiation of migration. VP (Sigma) treatment in conjunction with serum starvation resulted in significant cell death, instead cells were treated with VP containing media only, without serum starvation. ECFCs were treated with mito C (Tocris) diluted in basal media during the serum starve, before migration. Phase images of migration were taken on a Leica DMi8 or Zeiss Axio Observer Z1. After 8–12 h cells were fixed for immunofluorescence.

Live migration was performed on ECFCs expressing mTomato or EGFP in confluent or sparse conditions on collagen-coated 35-mm dishes. GFP-expressing ECFCs were transfected with nontargeting control siRNA, whereas mTomato-expressing ECFCs were transfected with siRNA targeting YAP and TAZ. Cells were seeded in a polydimethylsiloxane stencil with 3 × 5-mm channels separated by 0.75-mm gaps. 2 h after plating, the barrier was released, and seeded regions were imaged in 15-min intervals for 10 h using a Zeiss Axio Observer Z1 inverted microscope with an automated stage. Cells were maintained in an incubation chamber at 37°C, 5% CO_2, and 95% relative humidity for the duration of the experiment.

Immunoprecipitation

ECFCs were grown to confluence on collage-coated 10-cm tissue culture dishes. Cells were washed once in PBS and then lysed in ice cold radioimmunoprecipitation assay (RIPA; Cell Signaling) buffer containing protease phosphatase inhibitor (Cell Signaling). Lysate was homogenized passing through a 22-G needle. Lysate was cleared of debris at 1,000 *g* for 10 min at 4°C. Total monoclonal mouse anti-MYPT1 (1:50; Santa Cruz; sc-514261) was incubated for 1 h followed by addition of protein G Plus-Agarose–conjugated beads (1:50; Santa Cruz; sc-2002) at 4°C overnight. Beads were pelleted and washed with RIPA buffer containing protease phosphatase inhibitors five times. Bead-bound MYPT1 was then resuspended in 40 µl of 2× SDS buffer (Sigma) and used for SDS-PAGE and immunoblot against total p-Serine.

Immunofluorescence

Cells were washed twice in EBM-2 and fixed in 4% paraformaldehyde (Alfa Aesar) diluted in cytoskeletal stabilization buffer containing 10 mM 2-(N-morpholino) ethanesulfonic acid, 150 mM potassium chloride, 3 mM magnesium chloride, 2 mM ethylene glycol-bis(β-aminoethyl ether)-N,N,N',N'-tetraacetic acid, and 0.3 M sucrose for 20 min at room temperature. Cells were permeabilized and blocked in PBS containing 0.03% Triton X-100 (Amresco) with 5% goat serum (Cell Signaling) for 1 h. Isolation of stable FAs in situ was done by adding 0.05% Triton X-100 to the cytoskeletal stabilization buffer to remove the soluble and weakly adhered fraction of FAs, as described previously (Yamashita et al., 2014).

Fixed samples were incubated with antibodies diluted in PBS with 1% BSA: monoclonal YAP antibody (1:200; Cell Signaling; 14074), polyclonal TAZ antibody (1:250; Cell Signaling; 4883), monoclonal Vinculin antibody (1:200; Cell Signaling; 13901), MLC (1:200; Cell Signaling; 3672), pMLC (1:200; Cell Signaling; 3675), α-tubulin (1:2,000; Cell Signaling; DM18), GM130 (1:200; Cell Signaling; D6B1), RAB7 (1:100; Cell Signaling; D95F2), FAK (1:100; Cell Signaling; 3285), pFAK (1:100; Cell Signaling; D20B1), paxillin (4 µg/ml; Abcam; 80578), polyclonal Alexa Fluor 594–conjugated anti-rabbit IgG (1:400; Cell Signaling; 8889), and polyclonal Alexa Fluor 488–conjugated anti-mouse IgG (1:400; Cell Signaling; 4408). F-actin was stained using Alexa Fluor 488–conjugated phalloidin (1 U/ml; Life Technologies), and G-actin was stained with Alexa Fluor 594–conjugated DNase I (0.3 µM; Life Technologies) for 15 min. Samples were mounted in ProLong Gold Antifade solution (Thermo Fisher).

Integrin endocytosis assay

β1-integrin endocytosis was performed as previously described (Ezratty et al., 2005) Integrin internalization was performed on ECFCs sparsely plated on collagen-coated glass coverslips. 24 h after transfection coverslips were inverted on to 50-µl full medium droplets with β1-integrin antibody (10 µg/liter; Abcam; 12G10) on UV-sterilized parafilm. Coverslips were then placed a 4°C for 45 min to allow β1-integrin antibody to target active surface integrins while preventing active integrin endocytosis. Coverslips were returned to 6-well plates with prewarmed full medium and washed three times with full medium at 37°C for 30 min to allow internalization of integrin-antibody conjugates. Coverslips were washed three times in 4°C EBM-2, pH 4.0, to denature any remaining surface-bound antibodies. Cells were briefly washed with physiological pH EBM-2, pH 7.4, twice, then fixed as previously described in cytoskeletal stabilization buffer. Antibody detection and additional immunostaining was performed as described in the previous section.

Single-cell nanoindentation

ECFC stiffness at different distances from the leading edge of migrating cells was tested using a PIUMA CHIARO nanoindenter system (Optics 11; Casey et al., 2017). A colloidal probe cantilever with a tip radius and spring constant of 9.5 µm and 0.068 N/m, respectively, with a loading velocity of 2 µm/s was used in this study. Before testing, the sensitivity calibration of the cantilever was conducted by indenting a hard surface (i.e., a Petri dish). In brief, cell stiffness at the leading edge of the wound and in 100-µm bins from the leading edge were tested. Two control and three YAP/TAZ-depleted samples were tested with a total indentation of 15–32 cells at each measuring location. A customized MATLAB code (The MathWorks, Inc.; Casey et al., 2017) was developed to determine contact points between the probe and cells and to identify Young's moduli of the cells using the Hertz contact model

$$F = \frac{16}{9} E R^{1/2} \partial^{3/2},$$

where F is applied force, δ is indentation depth, R is the radius of the colloidal probe, and E is Young's modulus of the cells. The cells were assumed to be incompressible (i.e., Poisson's ratio of 0.5).

Immunohistochemistry

Collagen matrices containing lectin-labeled endothelial cell were stained with 1:100 Alexa Fluor 647–conjugated mouse anti-human CD31 antibody (BD Pharmigen clone WM59) at 4°C overnight. Next, the samples were cut into 0.3–0.5-mm thick pieces and mounted onto Superfrost Plus Gold microscope glass slides (Thermo Fisher) with ProLong Gold Antifade solution with DAPI (Thermo Fisher). Fluorescent pictures of vessels were taken on an Olympus II confocal microscope.

Paraffin-embedded tissues were sectioned, deparaffinized, and rehydrated. Heat-induced epitope retrieval was performed by incubating sections in sub-boiling 10 mM citrate buffer, pH 6.0, for 10 min, followed by washes in deionized water. Non-specific binding was blocked using horse serum from the Vectastain elite avidin-biotin conjugation kit (Vector; ABC kit) and endogenous peroxidase activity was quenched using 0.3% hydrogen peroxide in deionized water. Sections were incubated overnight 4°C with antibodies targeting YAP (1:400), TAZ (1:400), CTGF (1:400), or Cyr61 (1:400). The ABC kit universal secondary and biotinylated HRP-containing reagents were added according to the manufacturer's instructions. Antibody conjugation was detected using ImmPACT DAB peroxidase substrate. Sections were counterstained with hematoxylin and eosin (Sigma), coverslipped, and imaged with a Nikon 90i.

F-/G-actin fractionation

Filamentous and monomeric actin were isolated from ECFCs using the In Vivo F-/G-Actin Isolation kit (Cytoskeleton Inc.) according to the manufacturer's instruction. ECFCs were lysed in prewarmed actin stabilization buffer and collected for ultracentrifugation at 37°C, 100,000 *g* for 1 h, pelleting the multimeric, filamentous actin, leaving the monomeric actin in the supernatant. The F-actin containing pellet was resuspended in depolymerization buffer to the same volume as the monomeric supernatant. Both actin fractions were then subjected to SDS-PAGE, and total β-actin in each fraction was analyzed by fluorescent Western. Data are reported as the ratio of F-actin to G-actin fluorescence.

Western blot

Cells were washed in ice-cold dPBS, then lysed in 2× lammeli buffer (Alfa Aeasar), 24–30 h after transfection. Lysate was denatured by boiling samples for 5 min, followed by centrifugation at 12,000 *g* for 15 min. Lysate was separated based on molecular weight using electrophoresis on precast 4–12% Clearpage SDS gels (CBS Scientific) in conjunction with a low-range molecular weight ladder (Amresco) in TEO-tricine running buffer (CBS Scientific). Proteins were transferred to polyvinylidene difluoride (PVDF) membranes (Amresco) in Tris-glycine transfer buffer (CBS Scientific). Membranes were washed in TBS with 0.05% tween-20 (TBST; GeneTex), blocked in 5% BSA in TBST for 1 h, and incubated overnight at 4°C with primary antibodies targeting YAP (1:250), TAZ (1:1,000), or GAPDH (1:2,000) diluted in blocking buffer. The following day, membranes were washed in TBST, followed by incubation with HRP-conjugated secondary (1:3,000; Cell Signaling; 7074) for 1 h at room temperature, washed in TBST, and detected with chemiluminescent substrate (Pierce). Images were taken on Chemi-Doc It^2 (UVP), and densitometry of bands were performed on UVP Chemi-Doc It software; semiquantitative comparisons were made after normalizing to GAPDH. Membranes were stripped using a mild stripping buffer, pH 2.2 (1.5% glycine, 1% tween-20, and 0.1% SDS; Amresco), twice, followed by repeated washes in PBS and TBST.

Fluorescent western was performed on F- and G-actin fraction experiments and in TAZ protein–level quantification after triple depletion of YAP, TAZ, and NUAK2. In brief, cells were lysed in RIPA buffer (Cell Signaling) homogenized by passage through a 22-G needle and mixed with SDS loading buffer (Sigma). Samples were processed for SDS-PAGE using 4–12% Bolt Bis-Tris gels (Invitrogen) in morpholino propane sulfonic acid running buffer (Invitrogen). Proteins were transferred from gels to low-fluorescent PVDF (Biorad) with Tris-Glycine buffer (Biorad). PVDF was blocked in either fluorescent blocking buffer (LI-COR Biosciences) or 5% BSA diluted in TBS. Primary antibodies p-Serine (1:40,000; Abcam; ab9332), β-actin (Cytoskeleton Inc.; 1:1,000), and TAZ (1:1000) were incubated overnight in blocking buffer with 0.1% tween-20. Proteins were identified by IRDye 800– or 680 (LI-COR Biosciences)–conjugated secondaries incubated in blocking buffer with 0.1% tween-20 and 0.01% SDS. Fluorescent Western blots were imaged using a LI-COR Odyssey imager. Protein expression was normalized to total protein loading detected by REVERT total protein stain (LI-COR Biosciences). Quantification was performed using Image Studio Lite (LI-COR Biosciences).

RT-qPCR

Total RNA was isolated and purified using the RNeasy mini kit (qiagen). 0.5 µg of total RNA was reversed transcribed using the TaqMan reverse transcription kit (Life Technologies) using the manufacturer's instructions in a thermal cycler eco (Eppendorf). cDNA was mixed with iTaq Universal SYBR supermix (Biorad) and 0.4 µM forward and reverse primers in wells of 96-well PCR plate (Table 1; Biorad), followed by amplification and quantification with in a CFX connect real-time PCR system (Biorad).

Table 1. **RT-qPCR primers**

Gene	Forward (5′-3′)	Reverse (5′-3′)
YAP	CAACTCCAACCAGCAGCAACA	GCAGCCTCTCCTTCTCCATCTG
TAZ	ACCCACCCACGATGACCCCA	GCACCCTAACCCCAGGCCAC
CTGF	AGGAGTGGGTGTGTGACGA	CCAGGCAGTTGGCTCTAATC
Cyr61	GAGTGGGTCTGTGACGAGGAT	GGTTGTATAGGATGCGAGGCT
NUAK2	GTCAATCCGGAAGGACAAAA	TCACGATCTTGCTGCTGTTC
ARHGAP28	CCTCCTCGTGATACCTGTGG	TTTATCCTGGGATGCGTCAGA
ARHGAP29	GGAATCAGAACGCAAGCAAAA TGCG	GGGATGCTGATTCAGCCTCTTGG
GAPDH	AGGGCTGCTTTTAACTCTGGT	CCCCACTTGATTTTGGAGGGA

Microscopy and image analysis

Epifluorescence images of fixed samples were taken on either a Leica DMi8 equipped with a monochromatic DFC365 FX (Leica) or Zeiss Axio Observer equipped with a monochromatic Axiocam 702 (Zeiss) at 23°C using 5× (NA: 0.16), 10× (NA: 0.3), 20× (NA: 0.8), 40× (NA: 0.6), and 63× (NA: 1.2) Chroma objectives. Data acquisition was performed using either Leica Application Suite X (LAS X) or ZEN imaging suite (Zeiss).

All image analysis (morphometrics, intensity measurements, and individual cell tracking) were performed using an open access National Institutes of Health (NIH) software platform, FIJI (Schindelin et al., 2012). Live migration tracking was performed using a semiautomated tracking algorithm, TrackMate (Tinevez et al., 2017). Cells within 100 µm of the leading cell were considered front cells; all other cells were considered trailing.

Golgi polarization relative to wound edge was found by finding the angle between the horizontal direction of migration and the position vector between the centroid of nuclei and the associated Golgi in MATLAB using positional information obtained in ImageJ (NIH). Leading edge cells were defined as cells with 50 µm of the front-most cell.

YAP and TAZ activation as a function of cell density was performed on images of cells up to 1.2 mm from the actively migrating front. Images were binned into adjacent 100- × 950-µm ROIs, starting at the leading cell. Total and activated YAP or TAZ is the total integrated fluorescent intensity in an ROI, with or without the nuclear fraction digitally removed. Cell area in an ROI is the average area of five cells per ROI, and density is the number of DAPI-stained nuclei across the ROI.

Fluorescent intensity of immunocytochemistry was measured in epiflourescent images. Single-cell fluorescence was measured in cells with minimal cell contact, at the leading edge, whereas FA morphometrics were performed in sparsely plated cells. Florescent intensity measurements were taken from cells across at least two independent experiments; measurements were taken from each sample and normalized by the average intensity of the control for the experiment.

Statistics

All statistical analyses were performed on GraphPad Prism 6 statistical analysis package. Data are presented with data points

were possible and mean ± SEM or box plots representing interquartile range with whiskers at minimum/maximum. Multiple comparisons were made using ANOVA with Tukey's post hoc test for pairwise comparisons of normally distributed homoscedastic data. Data were assumed to fit the ANOVA assumptions if the residuals of a dataset were normally distributed. Data that did not meet the ANOVA criteria were analyzed by Kruskal-Wallis with Dunn's post hoc test. Repeated significance indicator letters (e.g., a–a) signify $P > 0.05$, while groups with distinct indicators (a vs. b) signify $P < 0.05$. Letters denote significant differences between groups, P values <0.05 were considered significant, and exact P values for the comparison with highest significant P value is recorded in the figure legend. Comparisons between two datasets were made using Student's unpaired two-tailed *t* test, where asterisks denote significant differences where exact P values are reported in the figure legend.

Online supplemental material

Fig. S1 shows YAP and TAZ localization is sensitive to PA hydrogel rigidity in ECFCs. Fig. S2 shows that YAP and TAZ RNA expression are not significantly altered during cell migration and that YAP and TAZ do not act through expression of the growth factors CTGF, Cyr61, or SERPINE1 to promote ECFC motility. Fig. S3 shows that YAP and TAZ regulate cell morphology and FA morphology and composition and that these changes can be reversed by myosin inhibition. Fig. S4 shows that NUAK1/2 inhibition is able to partially restore cytoskeletal remodeling in YAP/TAZ-depleted cells and that depletion of YAP, TAZ, and NUAK2 together produces a similar amount of depletion as YAP and TAZ depletion alone. Fig. S5 shows that 2 µM VP can reduce the expression of YAP, TAZ, and the YAP/TAZ target genes CTGF, Cyr61, SERPINE1, and NUAK2. Also shown is that VP produces a similar cytoskeletal effect as transcriptional inhibition and YAP/TAZ depletion. Videos 1, 2, and 3 show live cell migration of siControl (EGFP) and siYAP/TAZ (mTomato) during collective cell migration. Videos 4 and 5 are phase contrast videos of siControl (Video 4) and siYAP/TAZ (Video 5) cell migration and show that YAP/TAZ-depleted cells have distinct protrusions that remain as the cell retracts from its current position.

Acknowledgments

We would like to thank William Chris Shelley for his technical assistance, Lance Davidson for insightful discussions, Jason Burdick for providing cells, and Ronen Marmorstein and Sunbin Deng for assistance with actin fractionation.

This project was supported in part by American Heart Association grant 16SDG31230034 (to J.D. Boerckel), by National Institutes of Health National Center for Advancing Translational Sciences grant UL1TR001108 (to J.D. Boerckel), by National Science Foundation grant 1435467 (to J.D. Boerckel), National Science Foundation-CAREER Award no. 1651385 (P. Zorlutuna), and by the National Science Foundation's Science and Technology Center for Engineering MechanoBiology, grant CMMI-1548571.

The authors declare no competing financial interests.

Author contributions: D.E. Mason, J.M. Collins, J.H. Dawahare, T.D. Nguyen, and Y. Lin performed the experiments. D.E. Mason and J.D. Boerckel conceived and designed the experiments and wrote the manuscript. S.L. Voytik-Harbin, P. Zorlutuna, and M.C. Yoder provided reagents, cells, instrumentation, and advice for completing experiments. J.H. Dawahare, T.D. Nguyen, Y. Lin, S.L. Voytik-Harbin, P. Zorlutuna, and M.C. Yoder reviewed and provided feedback on the manuscript.

Submitted: 12 June 2018
Revised: 29 November 2018
Accepted: 11 January 2019

References

Antecol, M.H., A. Darveau, N. Sonenberg, and B.B. Mukherjee. 1986. Altered biochemical properties of actin in normal skin fibroblasts from individuals predisposed to dominantly inherited cancers. *Cancer Res.* 46: 1867–1873.

Arjonen, A., J. Alanko, S. Veltel, and J. Ivaska. 2012. Distinct recycling of active and inactive β1 integrins. *Traffic.* 13:610–625. https://doi.org/10.1111/j.1600-0854.2012.01327.x

Asahara, T., T. Murohara, A. Sullivan, M. Silver, R. van der Zee, T. Li, B. Witzenbichler, G. Schatteman, and J.M. Isner. 1997. Isolation of putative progenitor endothelial cells for angiogenesis. *Science.* 275:964–967. https://doi.org/10.1126/science.275.5302.964

Bailey, J.L., P.J. Critser, C. Whittington, J.L. Kuske, M.C. Yoder, and S.L. Voytik-Harbin. 2011. Collagen oligomers modulate physical and biological properties of three-dimensional self-assembled matrices. *Biopolymers.* 95:77–93. https://doi.org/10.1002/bip.21537

Baker, M., S.D. Robinson, T. Lechertier, P.R. Barber, B. Tavora, G. D'Amico, D. T. Jones, B. Vojnovic, and K. Hodivala-Dilke. 2012. Use of the mouse aortic ring assay to study angiogenesis. *Nat. Protoc.* 7:89–104. https://doi.org/10.1038/nprot.2011.435

Banerjee, S., S.J. Buhrlage, H.-T. Huang, X. Deng, W. Zhou, J. Wang, R. Traynor, A.R. Prescott, D.R. Alessi, and N.S. Gray. 2014. Characterization of WZ4003 and HTH-01-015 as selective inhibitors of the LKB1-tumour-suppressor-activated NUAK kinases. *Biochem. J.* 457:215–225. https://doi.org/10.1042/BJ20131152

Bergert, M., T. Lendenmann, M. Zündel, A.E. Ehret, D. Panozzo, P. Richner, D. K. Kim, S.J.P. Kress, D.J. Norris, O. Sorkine-Hornung, et al. 2016. Confocal reference free traction force microscopy. *Nat. Commun.* 7:12814. https://doi.org/10.1038/ncomms12814

Boerckel, J.D., U.M. Chandrasekharan, M.S. Waitkus, E.G. Tillmaand, R. Bartlett, and P.E. Dicorleto. 2014. Mitogen-activated protein kinase phosphatase-1 promotes neovascularization and angiogenic gene expression. *Arterioscler. Thromb. Vasc. Biol.* 34:1020–1031. https://doi.org/10.1161/ATVBAHA.114.303403

Calvo, F., N. Ege, A. Grande-Garcia, S. Hooper, R.P. Jenkins, S.I. Chaudhry, K. Harrington, P. Williamson, E. Moeendarbary, G. Charras, and E. Sahai. 2013. Mechanotransduction and YAP-dependent matrix remodelling is required for the generation and maintenance of cancer-associated fibroblasts. *Nat. Cell Biol.* 15:637–646. https://doi.org/10.1038/ncb2756

Carlson, T.R., H. Hu, R. Braren, Y.H. Kim, and R.A. Wang. 2008. Cell-autonomous requirement for beta1 integrin in endothelial cell adhesion, migration and survival during angiogenesis in mice. *Development.* 135:2193–2202. https://doi.org/10.1242/dev.016378

Caroti, C.M., H. Ahn, H.F. Salazar, G. Joseph, S.B. Sankar, N.J. Willett, L.B. Wood, W.R. Taylor, and A.N. Lyle. 2017. A Novel Technique for Accelerated Culture of Murine Mesenchymal Stem Cells that Allows for Sustained Multipotency. *Sci. Rep.* 7:13334. https://doi.org/10.1038/s41598-017-13477-y

Casey, J., X. Yue, T.D. Nguyen, A. Acun, V.R. Zellmer, S. Zhang, and P. Zorlutuna. 2017. 3D hydrogel-based microwell arrays as a tumor microenvironment model to study breast cancer growth. *Biomed. Mater.* 12: 025009. https://doi.org/10.1088/1748-605X/aa5d5c

Chan, C.E., and D.J. Odde. 2008. Traction dynamics of filopodia on compliant substrates. *Science.* 322:1687–1691. https://doi.org/10.1126/science.1163595

Chen, C.-P., X. Chen, Y.-N. Qiao, P. Wang, W.-Q. He, C.-H. Zhang, W. Zhao, Y.-Q. Gao, C. Chen, T. Tao, et al. 2015. In vivo roles for myosin phosphatase targeting subunit-1 phosphorylation sites T694 and T852 in bladder smooth muscle contraction. *J. Physiol.* 593:681–700. https://doi.org/10.1113/jphysiol.2014.283853

Chen, P., K. Gupta, and A. Wells. 1994. Cell movement elicited by epidermal growth factor receptor requires kinase and autophosphorylation but is separable from mitogenesis. *J. Cell Biol.* 124:547–555. https://doi.org/10.1083/jcb.124.4.547

Choi, H.-J., H. Zhang, H. Park, K.-S. Choi, H.-W. Lee, V. Agrawal, Y.-M. Kim, and Y.-G. Kwon. 2015. Yes-associated protein regulates endothelial cell contact-mediated expression of angiopoietin-2. *Nat. Commun.* 6:6943. https://doi.org/10.1038/ncomms7943

Critser, P.J., S.T. Kreger, S.L. Voytik-Harbin, and M.C. Yoder. 2010. Collagen matrix physical properties modulate endothelial colony forming cell-derived vessels in vivo. *Microvasc. Res.* 80:23–30. https://doi.org/10.1016/j.mvr.2010.03.001

Damljanović, V., B.C. Lagerholm, and K. Jacobson. 2005. Bulk and micropatterned conjugation of extracellular matrix proteins to characterized polyacrylamide substrates for cell mechanotransduction assays. *Biotechniques.* 39:847–851. https://doi.org/10.2144/000112026

Dupont, S., L. Morsut, M. Aragona, E. Enzo, S. Giulitti, M. Cordenonsi, F. Zanconato, J. Le Digabel, M. Forcato, S. Bicciato, et al. 2011. Role of YAP/TAZ in mechanotransduction. *Nature.* 474:179–183. https://doi.org/10.1038/nature10137

Elosegui-Artola, A., R. Oria, Y. Chen, A. Kosmalska, C. Pérez-González, N. Castro, C. Zhu, X. Trepat, and P. Roca-Cusachs. 2016. Mechanical regulation of a molecular clutch defines force transmission and transduction in response to matrix rigidity. *Nat. Cell Biol.* 18:540–548. https://doi.org/10.1038/ncb3336

Enzo, E., G. Santinon, A. Pocaterra, M. Aragona, S. Bresolin, M. Forcato, D. Grifoni, A. Pession, F. Zanconato, G. Guzzo, et al. 2015. Aerobic glycolysis tunes YAP/TAZ transcriptional activity. *EMBO J.* 34:1349–1370. https://doi.org/10.15252/embj.201490379

Esnault, C., A. Stewart, F. Gualdrini, P. East, S. Horswell, N. Matthews, and R. Treisman. 2014. Rho-actin signaling to the MRTF coactivators dominates the immediate transcriptional response to serum in fibroblasts. *Genes Dev.* 28:943–958. https://doi.org/10.1101/gad.239327.114

Ezratty, E.J., M.A. Partridge, and G.G. Gundersen. 2005. Microtubule-induced focal adhesion disassembly is mediated by dynamin and focal adhesion kinase. *Nat. Cell Biol.* 7:581–590. https://doi.org/10.1038/ncb1262

Fernandez-Gonzalez, R., S.M. Simoes, J.-C. Röper, S. Eaton, and J.A. Zallen. 2009. Myosin II dynamics are regulated by tension in intercalating cells. *Dev. Cell.* 17:736–743. https://doi.org/10.1016/j.devcel.2009.09.003

Galli, G.G., M. Carrara, W.-C. Yuan, C. Valdes-Quezada, B. Gurung, B. Pepe-Mooney, T. Zhang, G. Geeven, N.S. Gray, W. de Laat, et al. 2015. YAP Drives Growth by Controlling Transcriptional Pause Release from Dynamic Enhancers. *Mol. Cell.* 60:328–337. https://doi.org/10.1016/j.molcel.2015.09.001

Gerhardt, H., M. Golding, M. Fruttiger, C. Ruhrberg, A. Lundkvist, A. Abramsson, M. Jeltsch, C. Mitchell, K. Alitalo, D. Shima, and C. Betsholtz. 2003. VEGF guides angiogenic sprouting utilizing endothelial tip cell filopodia. *J. Cell Biol.* 161:1163–1177. https://doi.org/10.1083/jcb.200302047

Goto, H., M. Nishio, Y. To, T. Oishi, Y. Miyachi, T. Maehama, H. Nishina, H. Akiyama, T.W. Mak, Y. Makii, et al. 2018. Loss of *Mob1a/b* in mice results in chondrodysplasia due to YAP1/TAZ-TEAD-dependent repression of SOX9. *Development.* 145:dev159244. https://doi.org/10.1242/dev.159244

Gupton, S.L., and C.M. Waterman-Storer. 2006. Spatiotemporal feedback between actomyosin and focal-adhesion systems optimizes rapid cell migration. *Cell.* 125:1361–1374. https://doi.org/10.1016/j.cell.2006.05.029

Hossain, Z., S.M. Ali, H.L. Ko, J. Xu, C.P. Ng, K. Guo, Z. Qi, S. Ponniah, W. Hong, and W. Hunziker. 2007. Glomerulocystic kidney disease in mice with a targeted inactivation of Wwtr1. *Proc. Natl. Acad. Sci. USA.* 104:1631–1636. https://doi.org/10.1073/pnas.0605266104

Ichida, M., Y. Yui, K. Yoshioka, T. Tanaka, T. Wakamatsu, H. Yoshikawa, and K. Itoh. 2011. Changes in cell migration of mesenchymal cells during osteogenic differentiation. *FEBS Lett.* 585:4018–4024. https://doi.org/10.1016/j.febslet.2011.11.014

Ingram, D.A., L.E. Mead, H. Tanaka, V. Meade, A. Fenoglio, K. Mortell, K. Pollok, M.J. Ferkowicz, D. Gilley, and M.C. Yoder. 2004. Identification of a novel hierarchy of endothelial progenitor cells using human peripheral and umbilical cord blood. *Blood.* 104:2752–2760. https://doi.org/10.1182/blood-2004-04-1396

Ingram, D.A., L.E. Mead, D.B. Moore, W. Woodard, A. Fenoglio, and M.C. Yoder. 2005. Vessel wall-derived endothelial cells rapidly proliferate because they contain a complete hierarchy of endothelial progenitor cells. *Blood.* 105:2783–2786. https://doi.org/10.1182/blood-2004-08-3057

Kegelman, C.D., D.E. Mason, J.H. Dawahare, D.J. Horan, G.D. Vigil, S.S. Howard, A.G. Robling, T.M. Bellido, and J.D. Boerckel. 2018. Skeletal cell YAP and TAZ combinatorially promote bone development. *FASEB J.* 32:2706–2721. https://doi.org/10.1096/fj.201700872R

Kim, J., Y.H. Kim, J. Kim, D.Y. Park, H. Bae, D.-H. Lee, K.H. Kim, S.P. Hong, S.P. Jang, Y. Kubota, et al. 2017a. YAP/TAZ regulates sprouting angiogenesis and vascular barrier maturation. *J. Clin. Invest.* 127:3441–3461. https://doi.org/10.1172/JCI93825

Kim, M., T. Kim, R.L. Johnson, and D.-S. Lim. 2015. Transcriptional co-repressor function of the hippo pathway transducers YAP and TAZ. *Cell Reports.* 11:270–282. https://doi.org/10.1016/j.celrep.2015.03.015

Kim, T., D. Hwang, D. Lee, J.H. Kim, S.Y. Kim, and D.S. Lim. 2017b. MRTF potentiates TEAD-YAP transcriptional activity causing metastasis. *EMBO J.* 36:520–535. https://doi.org/10.15252/embj.201695137

Kolega, J. 2003. Asymmetric distribution of myosin IIB in migrating endothelial cells is regulated by a rho-dependent kinase and contributes to tail retraction. *Mol. Biol. Cell.* 14:4745–4757. https://doi.org/10.1091/mbc.e03-04-0205

Kreger, S.T., B.J. Bell, J. Bailey, E. Stites, J. Kuske, B. Waisner, and S.L. Voytik-Harbin. 2010. Polymerization and matrix physical properties as important design considerations for soluble collagen formulations. *Biopolymers.* 93:690–707. https://doi.org/10.1002/bip.21431

Kupfer, A., D. Louvard, and S.J. Singer. 1982. Polarization of the Golgi apparatus and the microtubule-organizing center in cultured fibroblasts at the edge of an experimental wound. *Proc. Natl. Acad. Sci. USA.* 79:2603–2607. https://doi.org/10.1073/pnas.79.8.2603

Lee, S.W., and J.J. Otto. 1996. Differences in turnover rates of vinculin and talin caused by viral transformation and cell density. *Exp. Cell Res.* 227:352–359. https://doi.org/10.1006/excr.1996.0284

Lei, Q.-Y., H. Zhang, B. Zhao, Z.-Y. Zha, F. Bai, X.-H. Pei, S. Zhao, Y. Xiong, and K.-L. Guan. 2008. TAZ promotes cell proliferation and epithelial-mesenchymal transition and is inhibited by the hippo pathway. *Mol. Cell. Biol.* 28:2426–2436. https://doi.org/10.1128/MCB.01874-07

Lin, C., E. Yao, K. Zhang, X. Jiang, S. Croll, K. Thompson-Peer, and P.-T. Chuang. 2017. YAP is essential for mechanical force production and epithelial cell proliferation during lung branching morphogenesis. *eLife.* 6:e21130. https://doi.org/10.7554/eLife.21130

Liu, F., D. Lagares, K.M. Choi, L. Stopfer, A. Marinković, V. Vrbanac, C.K. Probst, S.E. Hiemer, T.H. Sisson, J.C. Horowitz, et al. 2015. Mechanosignaling through YAP and TAZ drives fibroblast activation and fibrosis. *Am. J. Physiol. Lung Cell. Mol. Physiol.* 308:L344–L357. https://doi.org/10.1152/ajplung.00300.2014

Liu-Chittenden, Y., B. Huang, J.S. Shim, Q. Chen, S.-J. Lee, R.A. Anders, J.O. Liu, and D. Pan. 2012. Genetic and pharmacological disruption of the TEAD-YAP complex suppresses the oncogenic activity of YAP. *Genes Dev.* 26:1300–1305. https://doi.org/10.1101/gad.192856.112

Luo, T., K. Mohan, P.A. Iglesias, and D.N. Robinson. 2013. Molecular mechanisms of cellular mechanosensing. *Nat. Mater.* 12:1064–1071. https://doi.org/10.1038/nmat3772

Martin, A.F., M. Rabinowitz, R. Blough, G. Prior, and R. Zak. 1977. Measurements of half-life of rat cardiac myosin heavy chain with leucyl-tRNA used as precursor pool. *J. Biol. Chem.* 252:3422–3429.

Medina, R.J., C.L. Barber, F. Sabatier, F. Dignat-George, J.M. Melero-Martin, K. Khosrotehrani, O. Ohneda, A.M. Randi, J.K.Y. Chan, T. Yamaguchi, et al. 2017. Endothelial Progenitors: A Consensus Statement on Nomenclature. *Stem Cells Transl. Med.* 6:1316–1320. https://doi.org/10.1002/sctm.16-0360

Medjkane, S., C. Perez-Sanchez, C. Gaggioli, E. Sahai, and R. Treisman. 2009. Myocardin-related transcription factors and SRF are required for cytoskeletal dynamics and experimental metastasis. *Nat. Cell Biol.* 11:257–268. https://doi.org/10.1038/ncb1833

Moroishi, T., H.W. Park, B. Qin, Q. Chen, Z. Meng, S.W. Plouffe, K. Taniguchi, F.-X. Yu, M. Karin, D. Pan, and K.-L. Guan. 2015. A YAP/TAZ-induced feedback mechanism regulates Hippo pathway homeostasis. *Genes Dev.* 29:1271–1284. https://doi.org/10.1101/gad.262816.115

Nardone, G., J. Oliver-De La Cruz, J. Vrbsky, C. Martini, J. Pribyl, P. Skládal, M. Pešl, G. Caluori, S. Pagliari, F. Martino, et al. 2017. YAP regulates cell

mechanics by controlling focal adhesion assembly. *Nat. Commun.* 8: 15321. https://doi.org/10.1038/ncomms15321

Neto, F., A. Klaus-Bergmann, Y.-T. Ong, S. Alt, A.-C. Vion, A. Szymborska, J.R. Carvalho, I. Hollfinger, E. Bartels-Klein, C.A. Franco, et al. 2018. YAP and TAZ regulate adherens junction dynamics and endothelial cell distribution during vascular development. *eLife.* 7:e31037. https://doi.org/10.7554/eLife.31037

O'Brien, T.P., G.P. Yang, L. Sanders, and L.F. Lau. 1990. Expression of cyr61, a growth factor-inducible immediate-early gene. *Mol. Cell. Biol.* 10: 3569–3577. https://doi.org/10.1128/MCB.10.7.3569

Oakes, P.W., Y. Beckham, J. Stricker, and M.L. Gardel. 2012. Tension is required but not sufficient for focal adhesion maturation without a stress fiber template. *J. Cell Biol.* 196:363–374. https://doi.org/10.1083/jcb.201107042

Otsubo, K., H. Goto, M. Nishio, K. Kawamura, S. Yanagi, W. Nishie, T. Sasaki, T. Maehama, H. Nishina, K. Mimori, et al. 2017. MOB1-YAP1/TAZ-NKX2.1 axis controls bronchioalveolar cell differentiation, adhesion and tumour formation. *Oncogene.* 36:4201–4211. https://doi.org/10.1038/onc.2017.58

Ozanne, B.W., H.J. Spence, L.C. McGarry, and R.F. Hennigan. 2007. Transcription factors control invasion: AP-1 the first among equals. *Oncogene.* 26:1–10. https://doi.org/10.1038/sj.onc.1209759

Pasapera, A.M., I.C. Schneider, E. Rericha, D.D. Schlaepfer, and C.M. Waterman. 2010. Myosin II activity regulates vinculin recruitment to focal adhesions through FAK-mediated paxillin phosphorylation. *J. Cell Biol.* 188:877–890. https://doi.org/10.1083/jcb.200906012

Pepper, M.S., A.P. Sappino, R. Montesano, L. Orci, and J.-D. Vassalli. 1992. Plasminogen activator inhibitor-1 is induced in migrating endothelial cells. *J. Cell. Physiol.* 153:129–139. https://doi.org/10.1002/jcp.1041530117

Polte, T.R., G.S. Eichler, N. Wang, and D.E. Ingber. 2004. Extracellular matrix controls myosin light chain phosphorylation and cell contractility through modulation of cell shape and cytoskeletal prestress. *Am. J. Physiol. Cell Physiol.* 286:C518–C528. https://doi.org/10.1152/ajpcell.00280.2003

Porazinski, S., H. Wang, Y. Asaoka, M. Behrndt, T. Miyamoto, H. Morita, S. Hata, T. Sasaki, S.F.G. Krens, Y. Osada, et al. 2015. YAP is essential for tissue tension to ensure vertebrate 3D body shape. *Nature.* 521:217–221. https://doi.org/10.1038/nature14215

Qiao, Y., J. Chen, Y.B. Lim, M.L. Finch-Edmondson, V.P. Seshachalam, L. Qin, T. Jiang, B.C. Low, H. Singh, C.T. Lim, and M. Sudol. 2017. YAP Regulates Actin Dynamics through ARHGAP29 and Promotes Metastasis. *Cell Reports.* 19:1495–1502. https://doi.org/10.1016/j.celrep.2017.04.075

Reinhart-King, C.A., M. Dembo, and D.A. Hammer. 2003. Endothelial cell traction forces on RGD-derivatized polyacrylamide substrata. *Langmuir.* 19:1573–1579. https://doi.org/10.1021/la026142j

Rigort, A., J. Grünewald, V. Herzog, and G. Kirfel. 2004. Release of integrin macroaggregates as a mechanism of rear detachment during keratinocyte migration. *Eur. J. Cell Biol.* 83:725–733. https://doi.org/10.1078/0171-9335-00431

Roan, E., K.R. Wilhelm, and C.M. Waters. 2015. Kymographic Imaging of the Elastic Modulus of Epithelial Cells during the Onset of Migration. *Biophys. J.* 109:2051–2057. https://doi.org/10.1016/j.bpj.2015.10.005

Rodda, S.J., and A.P. McMahon. 2006. Distinct roles for Hedgehog and canonical Wnt signaling in specification, differentiation and maintenance of osteoblast progenitors. *Development.* 133:3231–3244. https://doi.org/10.1242/dev.02480

Ryseck, R.P., H. Macdonald-Bravo, M.G. Mattéi, and R. Bravo. 1991. Structure, mapping, and expression of fisp-12, a growth factor-inducible gene encoding a secreted cysteine-rich protein. *Cell Growth Differ.* 2:225–233.

Sakabe, M., J. Fan, Y. Odaka, N. Liu, A. Hassan, X. Duan, P. Stump, L. Byerly, M. Donaldson, J. Hao, et al. 2017. YAP/TAZ-CDC42 signaling regulates vascular tip cell migration. *Proc. Natl. Acad. Sci. USA.* 114:10918–10923. https://doi.org/10.1073/pnas.1704030114

Schindelin, J., I. Arganda-Carreras, E. Frise, V. Kaynig, M. Longair, T. Pietzsch, S. Preibisch, C. Rueden, S. Saalfeld, B. Schmid, et al. 2012. Fiji: an open-source platform for biological-image analysis. *Nat. Methods.* 9: 676–682. https://doi.org/10.1038/nmeth.2019

Shen, Z., and B.Z. Stanger. 2015. YAP regulates S-phase entry in endothelial cells. *PLoS One.* 10:e0117522. https://doi.org/10.1371/journal.pone.0117522

Shen, T.-L., A.Y.-J. Park, A. Alcaraz, X. Peng, I. Jang, P. Koni, R.A. Flavell, H. Gu, and J.-L. Guan. 2005. Conditional knockout of focal adhesion kinase in endothelial cells reveals its role in angiogenesis and vascular development in late embryogenesis. *J. Cell Biol.* 169:941–952. https://doi.org/10.1083/jcb.200411155

Tinevez, J.-Y., N. Perry, J. Schindelin, G.M. Hoopes, G.D. Reynolds, E. Laplantine, S.Y. Bednarek, S.L. Shorte, and K.W. Eliceiri. 2017. TrackMate: An open and extensible platform for single-particle tracking. *Methods.* 115:80–90. https://doi.org/10.1016/j.ymeth.2016.09.016

Totsukawa, G., Y. Wu, Y. Sasaki, D.J. Hartshorne, Y. Yamakita, S. Yamashiro, and F. Matsumura. 2004. Distinct roles of MLCK and ROCK in the regulation of membrane protrusions and focal adhesion dynamics during cell migration of fibroblasts. *J. Cell Biol.* 164:427–439. https://doi.org/10.1083/jcb.200306172

Vallenius, T., K. Vaahtomeri, B. Kovac, A.-M. Osiceanu, M. Viljanen, and T.P. Mäkelä. 2011. An association between NUAK2 and MRIP reveals a novel mechanism for regulation of actin stress fibers. *J. Cell Sci.* 124:384–393. https://doi.org/10.1242/jcs.072660

Wada, K., K. Itoga, T. Okano, S. Yonemura, and H. Sasaki. 2011. Hippo pathway regulation by cell morphology and stress fibers. *Development.* 138:3907–3914. https://doi.org/10.1242/dev.070987

Wang, N., I.M. Tolić-Nørrelykke, J. Chen, S.M. Mijailovich, J.P. Butler, J.J. Fredberg, and D. Stamenović. 2002. Cell prestress. I. Stiffness and prestress are closely associated in adherent contractile cells. *Am. J. Physiol. Cell Physiol.* 282:C606–C616. https://doi.org/10.1152/ajpcell.00269.2001

Wang, X., A. Freire Valls, G. Schermann, Y. Shen, I.M. Moya, L. Castro, S. Urban, G.M. Solecki, F. Winkler, L. Riedemann, et al. 2017. YAP/TAZ Orchestrate VEGF Signaling during Developmental Angiogenesis. *Dev. Cell.* 42:462–478.e7. https://doi.org/10.1016/j.devcel.2017.08.002

Weiss, L., and M.K. Chang. 1973. Some effects of actinomycin D, cycloheximde and puromycin on cell adhesion. *J. Cell Sci.* 12:655–664.

Whittington, C.F., M.C. Yoder, and S.L. Voytik-Harbin. 2013. Collagen-polymer guidance of vessel network formation and stabilization by endothelial colony forming cells in vitro. *Macromol. Biosci.* 13:1135–1149. https://doi.org/10.1002/mabi.201300128

Wu, Z., S.V. Plotnikov, A.Y. Moalim, C.M. Waterman, and J. Liu. 2017. Two Distinct Actin Networks Mediate Traction Oscillations to Confer Focal Adhesion Mechanosensing. *Biophys. J.* 112:780–794. https://doi.org/10.1016/j.bpj.2016.12.035

Xin, M., Y. Kim, L.B. Sutherland, M. Murakami, X. Qi, J. McAnally, E.R. Porrello, A.I. Mahmoud, W. Tan, J.M. Shelton, et al. 2013. Hippo pathway effector Yap promotes cardiac regeneration. *Proc. Natl. Acad. Sci. USA.* 110:13839–13844. https://doi.org/10.1073/pnas.1313192110

Yamamoto, H., S. Takashima, Y. Shintani, S. Yamazaki, O. Seguchi, A. Nakano, S. Higo, H. Kato, Y. Liao, Y. Asano, et al. 2008. Identification of a novel substrate for TNFalpha-induced kinase NUAK2. *Biochem. Biophys. Res. Commun.* 365:541–547. https://doi.org/10.1016/j.bbrc.2007.11.013

Yamashita, H., T. Ichikawa, D. Matsuyama, Y. Kimura, K. Ueda, S.W. Craig, I. Harada, and N. Kioka. 2014. The role of the interaction of the vinculin proline-rich linker region with vinexin α in sensing the stiffness of the extracellular matrix. *J. Cell Sci.* 127:1875–1886. https://doi.org/10.1242/jcs.133645

Zagórska, A., M. Deak, D.G. Campbell, S. Banerjee, M. Hirano, S. Aizawa, A.R. Prescott, and D.R. Alessi. 2010. New roles for the LKB1-NUAK pathway in controlling myosin phosphatase complexes and cell adhesion. *Sci. Signal.* 3:ra25–ra25. https://doi.org/10.1126/scisignal.2000616